UC Davis
UC Davis Electronic Theses and Dissertations

Title

DFT and Microkinetic Modeling Study of Two-Carbon Product Pathways in the Partial Oxidation of Methanol over Silver

Permalink

https://escholarship.org/uc/item/5rf7s7bm

Author

Shaw, Austin

Publication Date

2021

Peer reviewed|Thesis/dissertation

DFT and Microkinetic Modeling Study of Two-Carbon Product Pathways in the Partial Oxidation of
Methanol over Silver

By

AUSTIN SHAW
THESIS

Submitted in partial satisfaction of the requirements for the degree of

MASTER OF SCIENCE

in

Chemical Engineering

in the

OFFICE OF GRADUATE STUDIES

of the

UNIVERSITY OF CALIFORNIA

DAVIS

Approved:

Dr. Ambarish Kulkarni, Chair

Dr. Roland Faller

Dr. Ahmet Palazoglu

Committee in Charge

2021

Table of Contents

List of Figures

iv

List of Tables

Acknowledgements

I would like to acknowledge and express my gratitude to the following individuals and institutions whose support have made my education possible. Firstly, I want to thank my advisor, Dr. Ambarish Kulkarni, for his support of my research and his patience and knowledge. I would also like to express my gratitude to my thesis committee members, Dr. Roland Faller and Dr. Ahmet Palazoglu, for their time and effort in reviewing this thesis.

I acknowledge the University of California at Davis, specifically the Department of Chemical Engineering, for funding my education and allowing me to serve as a researcher and teaching assistant. I would also like to acknowledge the US Department of Energy (DOE) for their financial support of my research.

I wish to thank the members of Dr. Kulkarni and Dr. Coleman Kronawitter's research groups for their feedback and assistance throughout the project. I am also indebted to our experimental collaborators at Sandia National Laboratory whose innovative work made this project possible.

I would also like to extend my gratitude to Dr. Ashok Prasad at Colorado State University, for his mentorship and support of my undergraduate research, and for encouraging me to pursue my educational goals.

Finally, I would like to thank my family and friends for their guidance and encouragement during my time in graduate school. Without your levity, unconditional support, and advice, this work would not have been possible.

Abstract

Though much of the reaction mechanism of the oxidative conversion of methanol to formaldehyde on silver is well understood, recent discovery of acetaldehyde as a product of methanol oxidation over a silver catalyst has led to questions about the potential for carbon-carbon coupling reactions. This has created an opportunity for theoretical research to identify the mechanism for the formation of acetaldehyde and other two-carbon products. Analysis of density functional theory (DFT) data from available literature largely supports previously proposed network of elementary steps, which include pathways for formaldehyde, carbon monoxide and carbon dioxide production. DFT calculations in this work and microkinetic modeling study provide theoretical explanations of reaction mechanisms that form acetaldehyde, methyl formate, and dimethyl ether. Free energy calculations show that the activation energy of intermediate coupling reactions could play a central role in controlling selectivities of two-carbon species, favoring the synthesis of methyl formate. Microkinetic modeling reveals that direct formation of acetaldehyde and methyl formate, as well as the synthesis of dimethyl ether, are coverage-limited by CHO^* and CH_3^*, respectively. This work introduces a set of reaction mechanisms which likely explain experimental observations of two-carbon products in the partial oxidation of methanol over silver.

1. Introduction and Literature Review

1.1 Reaction

Formaldehyde is an important precursor for a range of applications, including resins and a range of chemicals used in industries such as construction, automotive, aviation, pharmaceuticals, and cosmetics. The manufacture of formaldehyde has primarily utilized silver catalyst since 1923, and silver continues to be one of the most used catalysts for industrial applications, along with iron-oxide-molybdenum-oxide catalyst [1].

1.2 Mechanistic Studies

There have been extensive experimental studies into the mechanism of the oxidation of methanol to formaldehyde. Methanol is not reacted in the absence of oxygen [2]–[5]. Early studies [2], [6] indicated that methanol adsorption was assisted by adsorbed or sub-surface oxygen species. These conclusions were supported by later isotope labeling and temperature-programmed reactor (TPR) studies by Wachs and Madix's group showing that methanol dissociatively adsorbs in the presence of monatomic surface oxygen to yield a methoxy intermediate and surface hydroxide [3], [7]. In situ surface Raman spectroscopy also support this conclusion [4]. The detection of abundant surface formate intermediate by [4] and temperature-programmed desorption (TPD) studies showing CO_2 desorption and formate formation at the same temperature by [7] suggest that formate decomposition is likely a surface phenomenon. Formaldehyde may be converted to formate groups and other intermediates that are quickly converted and desorbed as gaseous products CO and CO_2 [4], [7]. TPR and TPD studies conducted for Au, Ag, and Cu suggest that these undesirable reactions are favored by (1) longer residence times of formaldehyde on the surface and (2) remaining oxygen species present on the surface or in the topmost layer of a reconstructed silver lattice [3], [7]. These conclusions are

also supported by Raman spectroscopic experiment [4] and reactor study [8] . Some have

proposed that the decomposition of formaldehyde is a gas-phase reaction [9], [10].

Experiments over the years have detected two-carbon (C_2) species as byproducts of this

reaction, primarily methyl formate, CH_3COOH [7], [10], [11], which is known to be an impurity

in industrial implementations [1], along with dimethyl ether and acetone. TPR and isotope

labeling studies showed that methyl formate is a major product following co-adsorption of

formaldehyde and methanol on $Ag(110)$ and that methyl formate likely originates from a

hemiacetal alcoholate surface complex ($H_2COOCH_3^*$) formed by surface intermediate coupling of

a formaldehyde oxygen and a methoxy carbon:

$$1. \qquad H_2CO^* \ + \ CH_3O^* \ \leftrightarrow \ H_2COOCH_3^*$$

$$2. \qquad H_2COOCH_3^* \ \leftrightarrow \ HCOOCH_3^* \ + \ H^*$$

$$3. \qquad HCOOCH_3^* \ \rightarrow \ HCOOCH_3(g)$$

Wachs and Madix suggest in [7] that hydride transfer to the surface (or to a nucleophilic oxygen

or hydroxy surface species) is likely the rate-limiting step. Though dimethyl ether has been

observed as a product of this reaction, no theoretical study has been conducted on this aspect.

1.3 Temperature Dependence and Oxygen Species

Methanol partial oxidation has a light-off temperature of about 500-570 K [8]–[10], [12].

The oxidation of methanol to formaldehyde shows a strong temperature dependence. In studies

conducted on fresh Ag catalyst particles, three distinct regimes of oxidation kinetics occurred:

(1) a region of low formaldehyde selectivity and mostly CO_2 by-product between 550 and 700 K,

(2) a region of very low activity between 700 K and 850 K, and (3) a region of more selective

formaldehyde formation with mostly CO by-product above 850 K [9], [13]. Further cycles of

methanol oxidation caused morphological changes to the catalyst surface that caused the

trimodal temperature dependence to disappear, indicating that industrial applications for this reaction, which re-use silver catalyst for multiple weeks, likely do not show this extreme temperature dependence. Other studies have also found temperature-conversion profiles which show different regimes of catalyst activity [10]. However, this finding has introduced a paradigm of methanol oxidation kinetics based on the existence of distinct oxygen phases in silver, which favor different temperature ranges and are implicated in distinct pathways of methanol oxidation [10], [13], [14]. These species are (1) O_α, adsorbed species oxygen, which predominates at lower temperatures, (2) O_β, bulk-dissolved oxygen, which is stable at lower temperatures and at higher temperatures diffuses to the surface to form (3) O_γ, oxygen atoms embedded in the top layer of the silver. These phases have been detected by a variety of spectroscopic techniques [14]. The existence of these subsurface species causes significant morphological changes to catalyst surfaces, including sintering, as well as the formation of pinholes through disruptive subsurface reactions between hydrogen and oxygen to form water [9], [15].

Some authors have proposed that two competing mechanisms for formaldehyde synthesis occur at two distinct oxygen sites on the surface: unselective oxidation of methanol by O_α (dominant at lower temperatures) and selective oxy-dehydrogenation of methanol by surface-layer O_γ (dominant at higher temperatures) [9], [13]. Nevertheless, authors have been able to replicate experimental results over a range of temperatures using only one form of adsorbed oxygen in microkinetic modeling [16].

1.4 Operando Methods

Kinetic experiments in heterogeneous catalysis have often been conducted using ultrahigh vacuum (UHV) environments, but more recent study has made use of operando techniques that probe catalysis phenomena at relevant pressures. Although UHV studies can provide great

insight into mechanistic details of surface reactions, real-world reactions conducted at higher pressures involved a different operating regime, with higher surface coverages, greater kinetic energies and probabilities of collision, as well as gas-phase transport effects [12]. Operando techniques also give information on the catalyst surface and surface chemistry at operating conditions, with such technologies as X-ray spectroscopies, Fourier-transform infrared spectroscopy, solid-state NMR, and Raman and UV-vis spectroscopies [12]. Zhou and coworkers, who are our collaborators at Sandia National Laboratories, have developed an experimental system consisting of planar laser-induced fluorescence (PLIF) imaging complimented by Raman and mass spectroscopy probes to generate high spatial and high temporal resolution temperature and composition profiles for stable species and low-resolution data for unstable intermediates. A recent study of theirs [12] yielded rich kinetic information for the partial oxidation of methanol over silver which we aimed to validate with microkinetic modeling.

These experiments gave species-resolved visualizations of laminar boundary layers in the gas-phase with CH_2O-PLIF. 1-D Raman spectroscopy (taken at 9 different heights and interpolated) gave data that showed spatial temperature and concentration distributions for major species. A separate mass spectroscopy experiment setup gave data for universal detection of species in the reaction, which included contributions from species such as methanol, oxygen, water, CO_2, and CH_2O. Methyl formate, as well as several stable and unstable C_2-species products and intermediates, were also detected. Notably, acetaldehyde was detected for the first time in the history of experimental study of this reaction [12].

1.6 Microkinetic Modeling

Microkinetic modeling is an increasingly popular technique for extracting kinetic information from experimental results, which makes use of computational tools to solve systems of differential equations for modeling complex reaction networks. Thermodynamic parameters are calculated with theory or taken from tabulated data. The reaction system is modeled with a set of mole balance equations that take the form of ordinary differential equations (ODEs). When complexity and accuracy is appropriately balanced with computational tractability and simplicity, microkinetic modeling can be an effective tool for insight into reaction mechanisms [17]. This work makes use of DFT data and elementary steps from an existing microkinetic model from Aljama and coworkers in 2016 [18], to which we added additional steps for formation of C_2 products.

1.7 Motivation

Mass spectrometry measurements by our Sandia collaborators have shown for the first time that carbon-carbon coupling steps may be possible in this reaction network, specifically for the formation of acetaldehyde. Additionally, there is no existing microkinetic model that includes mechanisms for the formation of other two-carbon product species methyl formate and dimethyl ether. To better understand the mechanism of this reaction and the role of carbon-carbon coupling in forming acetaldehyde, RPBE-D3 [19]plane-wave DFT calculations and microkinetic modeling studies were conducted.

2. Methodology

2.1 Density Functional Theory

First-principles calculations were performed using plane-wave DFT in the Vienna Ab-Initio Simulation Package (VASP) using the projector-augmented wave (PAW) method. Electronic cores were represented with PAW PBE pseudopotentials [20]. The Atomic Simulation Environment (ASE) [21] was used with VASP code [22]–[25]. The RPBE-D3 GGA functional, which has been shown to accurately calculate chemisorption energies on metal surfaces [26], was used for adsorption and vibration calculations. A plane-wave energy cutoff of 500 eV was used. The bulk lattice constant of Ag was 4.212 Å, calculated with the RPBE functional, which is in relative agreement with the experimental value of 4.086 ± 0.041 Å [27] (error of 3.084 %).

Testing revealed that relaxations with RPBE-D3 caused unphysical compression of the silver surface, so all geometric relaxations were carried out with the RPBE functional, followed by single point energy evaluations relying on the RPBE-D3 functional. This approach provides a good balance between predicting the correct lattice constants, while also including the effect of dispersion interactions.

For all surface DFT calculations, a 4x4x1 Monkhorst-Pack k-point mesh was used for integration over the Brillouin zone. The face-centered cubic Ag(111) surface was modeled by a 3x3x4 slab with periodic boundary conditions. The top two layers were optimized, while the bottom 2 layers remained fixed at the bulk lattice constants. The artificial stresses introduced by using these constraints may cause errors in DFT energies. A vacuum of 18 Å separated successive slabs. Refer to Figure 1 for an example unit cell. Geometry optimizations were implemented in ASE with Brent's method (scipy.optimize.minimize_scalar). The convergence

criterion for structural optimization was a maximum force of 0.03 eV/Å per atom. Convergence tests are in the appendix (A.1).
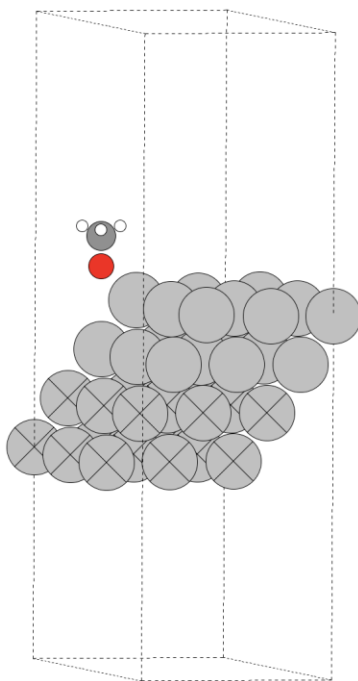
Figure 1. Unit cell of surface-bound methoxy used in DFT calculations.

Transition states were determined using the climbing image nudged elastic band (CI-NEB) method, with a convergence criterion of 0.05 eV/Å per atom. Three transition states discussed in this work are not converged to this level of accuracy: $CH_3O-CH_2O^*$ (Reaction 56 in Table 2), CH_3O-CHO^* (Rxn 57), and $CH_3OCHO-H--O^*$ (Rxn 65). They were, however, converged to 0.05 eV/Å at a lower plane-wave energy cutoff and k-point mesh. This inconsistency is noted in this thesis when relevant but is unlikely to affect our overall conclusions.

2.2 Reaction mechanism

Our model is based on the mechanism published in [18] (Reactions 1 through 55 in Table 1). Our model assumes that the surface role of Oxygen in the reaction is sufficiently described

with a single species O^*, or O_α (refer to A.3 for supporting DFT calculations). To account for

Zhou et al.'s observations of C_2 species [12], we included the set of elementary steps in Table 2.

The mechanism for methyl formate reaction is that introduced by Wachs and Madix in 1978 [7].

Dimethyl ether may form from surface coupling of methyl and methoxy species. In contrast with

these other species, acetaldehyde results from carbon-coupling between surface methyl species

and either surface CH_2O^* or CHO^*. Pathways for dehydrogenation include competing surface-,

O^*-, and OH^*-assisted steps.

Table 1: Elementary steps of base model from [18].

	Elementary Step
1	$CH_3OH + O^* + * \leftrightarrow CH_3O\text{-}H\text{-}O + * \leftrightarrow CH_3O^* + OH^*$
2	$CH_3OH + OH^* + * \leftrightarrow CH_3O\text{-}H\text{-}OH + * \leftrightarrow CH_3O^* + H_2O + *$
3	$CH_3O^* + O^* \leftrightarrow CH_2\text{-}H\text{-}O\text{-}\text{-}O + * \leftrightarrow CH_2O^* + OH^* + *$
4	$CH_3O^* + OH^* \leftrightarrow CH_2\text{-}H\text{-}O\text{-}\text{-}OH + * \leftrightarrow CH_2O^* + H_2O + * + *$
5	$CH_3OH + O^* + * \leftrightarrow CH_2\text{-}H\text{-}OH\text{-}\text{-}O + * \leftrightarrow CH_2OH^* + OH^*$
6	$CH_3OH + OH^* + * \leftrightarrow CH_2\text{-}H\text{-}OH\text{-}\text{-}OH + * \leftrightarrow CH_2OH^* + H_2O + *$
7	$CH_2OH^* + O^* \leftrightarrow CH_2O\text{-}H\text{-}O + * \leftrightarrow CH_2O^* + OH^*$
8	$CH_2OH^* + OH^* \leftrightarrow CH_2O\text{-}H\text{-}OH + * \leftrightarrow CH_2O^* + H_2O + *$
9	$CH_2OH^* + O^* \leftrightarrow CH\text{-}H\text{-}OH\text{-}\text{-}O + * \leftrightarrow CHOH^* + OH^*$
10	$CH_2OH^* + OH^* \leftrightarrow CH\text{-}H\text{-}OH\text{-}\text{-}OH + * \leftrightarrow CHOH^* + H_2O + *$
11	$CHOH^* + O^* \leftrightarrow CHO\text{-}H\text{-}O + * \leftrightarrow CHO^* + OH^*$
12	$CHOH^* + OH^* \leftrightarrow CHO\text{-}H\text{-}OH + * \leftrightarrow CHO^* + H_2O + *$
13	$CHOH^* + O^* \leftrightarrow C\text{-}H\text{-}OH\text{-}\text{-}O + * \leftrightarrow COH^* + OH^*$
14	$CHOH^* + OH^* \leftrightarrow C\text{-}H\text{-}OH\text{-}\text{-}OH + * \leftrightarrow COH^* + H_2O + *$
15	$COH^* + O^* \leftrightarrow CO\text{-}H\text{-}O + * \leftrightarrow CO^* + OH^*$
16	$COH^* + OH^* \leftrightarrow CO\text{-}H\text{-}OH + * \leftrightarrow CO^* + H_2O + *$
17	$CH_2O^* + O^* \leftrightarrow CH\text{-}H\text{-}O\text{-}\text{-}O + * \leftrightarrow CHO^* + OH^*$
18	$CH_2O^* + OH^* \leftrightarrow CH\text{-}H\text{-}O\text{-}\text{-}OH + * \leftrightarrow CHO^* + H_2O + *$
19	$CHO^* + O^* \leftrightarrow C\text{-}H\text{-}O\text{-}\text{-}O + * \leftrightarrow CO^* + OH^*$
20	$CHO^* + OH^* \leftrightarrow C\text{-}H\text{-}O\text{-}\text{-}OH + * \leftrightarrow CO^* + H_2O + *$
21	$CH_3OH + * + * \leftrightarrow CH_3O\text{-}H + * \leftrightarrow CH_3O^* + H^*$
22	$CH_3OH + * + * \leftrightarrow CH_2\text{-}H\text{-}OH + * \leftrightarrow CH_2OH^* + H^*$
23	$CH_3OH + * + * \leftrightarrow CH_3\text{-}OH + * \leftrightarrow CH_3 + OH^*$
24	$CH_3O^* + * \leftrightarrow CH_2\text{-}H\text{-}O + * \leftrightarrow CH_2O + H^*$

25	$CH_3O^* + * \leftrightarrow CH_3\text{-}O + * \leftrightarrow CH_3^* + O^*$
26	$CH_2O^* \leftrightarrow CH_2O^* \leftrightarrow CH_2O + *$
27	$CH_2O^* + * \leftrightarrow CH\text{-}H\text{-}O + * \leftrightarrow CHO^* + H^*$
28	$CH_2O^* + * \leftrightarrow CH_2\text{-}O + * \leftrightarrow CH_2^* + O^*$
29	$CHO^* + * \leftrightarrow H\text{-}CO + * \leftrightarrow CO^* + H^*$
30	$CHO^* + * \leftrightarrow CH\text{-}O + * \leftrightarrow CH^* + O^*$
31	$CH_2OH^* + * \leftrightarrow CH_2O\text{-}H + * \leftrightarrow CH_2O^* + H^*$
32	$CH_2OH^* + * \leftrightarrow CH\text{-}H\text{-}OH + * \leftrightarrow CHOH^* + H^*$
33	$CH_2OH^* + * \leftrightarrow CH_2\text{-}OH + * \leftrightarrow CH_2^* + OH^*$
34	$CHOH^* + * \leftrightarrow C\text{-}H\text{-}OH + * \leftrightarrow COH^* + H^*$
35	$CHOH^* + * \leftrightarrow CHO\text{-}H + * \leftrightarrow CHO^* + H^*$
36	$CHOH^* + * \leftrightarrow CH\text{-}OH + * \leftrightarrow CH^* + OH^*$
37	$COH^* + * \leftrightarrow CO\text{-}H + * \leftrightarrow CO^* + H^*$
38	$COH^* + * \leftrightarrow C\text{-}OH + * \leftrightarrow C^* + OH^*$
39	$CH_3^* + * \leftrightarrow CH_2\text{-}H + * \leftrightarrow CH_2^* + H^*$
40	$CH_2^* + * \leftrightarrow CH\text{-}H + * \leftrightarrow CH^* + H^*$
41	$CH^* + * \leftrightarrow C\text{-}H + * \leftrightarrow C^* + H^*$
42	$CH_3^* + O^* \leftrightarrow CH_2\text{-}H\text{-}\text{-}O + * \leftrightarrow CH_2^* + OH^*$
43	$CH_2^* + O^* \leftrightarrow CH\text{-}H\text{-}\text{-}O + * \leftrightarrow CH^* + OH^*$
44	$CH^* + O^* \leftrightarrow C\text{-}H\text{-}\text{-}O + * \leftrightarrow C^* + OH^*$
45	$CH_3^* + OH^* \leftrightarrow CH_2\text{-}H\text{-}\text{-}OH + * \leftrightarrow CH_2^* + * + H_2O$
46	$CH_2^* + OH^* \leftrightarrow CH\text{-}H\text{-}\text{-}OH + * \leftrightarrow CH^* + * + H_2O$
47	$CH^* + OH^* \leftrightarrow C\text{-}H\text{-}\text{-}OH + * \leftrightarrow C^* + * + H_2O$
48	$CO + * \leftrightarrow CO + * \leftrightarrow CO^*$
49	$CO_2 + * + * \leftrightarrow CO\text{-}O + * \leftrightarrow CO^* + O^*$
50	$CO^* + * \leftrightarrow C\text{-}O + * \leftrightarrow C^* + O^*$
51	$H_2O + * + * \leftrightarrow HO\text{-}H + * \leftrightarrow OH^* + H^*$
52	$OH^* + * \leftrightarrow O\text{-}H + * \leftrightarrow O^* + H^*$
53	$O_2 + * + * \leftrightarrow O\text{-}O + * \leftrightarrow O^* + O^*$
54	$H_2 + * + * \leftrightarrow H\text{-}H + * \leftrightarrow H^* + H^*$
55	$OH^* + OH^* \leftrightarrow HO\text{-}H\text{-}\text{-}O + * \leftrightarrow H_2O + O^* + *$

Table 2. Additional elementary steps for this work.

Acetaldehyde Pathway	
56	$CH_3^* + CH_2O^* \leftrightarrow H_3C\text{-}CH_2O^* + {}^* \leftrightarrow CH_3CH_2O^* + {}^*$
57	$CH_3^* + CHO^* \leftrightarrow H_3C\text{-}CHO^* + {}^* \leftrightarrow CH_3CHO^* + {}^*$
58	$CH_3CH_2O^* + {}^* \leftrightarrow CH_3CHO\text{-}H^* + {}^* \leftrightarrow CH_3CHO^* + H^*$

59	$CH_3CH_2O^* + O^* \leftrightarrow CH_3CHO\text{-}H\text{-}\text{-}O^* + ~^* \leftrightarrow CH_3CHO^* + OH^*$
60	$CH_3CH_2O^* + OH^* \leftrightarrow CH_3CHO\text{-}H\text{-}\text{-}OH^* + ~^* \leftrightarrow CH_3CHO^* + H_2O^*$
61	$CH_3CHO^* \leftrightarrow CH_3CHO(g) + ~^*$
Methyl Formate Pathway	
62	$CH_3O^* + CH_2O^* \leftrightarrow CH_3O\text{-}CH_2O^* + ~^* \leftrightarrow CH_3OCH_2O^* + ~^*$
63	$CH_3O^* + CHO^* \leftrightarrow CH_3O\text{-}CHO^* + ~^* \leftrightarrow CH_3COOH^* + ~^*$
64	$CH_3OCH_2O^* + ~^* \leftrightarrow CH_3OCHO\text{-}H^* + ~^* \leftrightarrow CH_3COOH^* + H^*$
65	$CH_3OCH_2O^* + O^* \leftrightarrow CH_3OCHO\text{-}H\text{-}\text{-}O^* + ~^* \leftrightarrow CH_3COOH^* + OH^*$
66	$CH_3OCH_2O^* + OH^* \leftrightarrow CH_3OCHO\text{-}H\text{-}\text{-}OH^* + ~^* \leftrightarrow CH_3COOH^* + H_2O^*$
67	$CH_3COOH^* \leftrightarrow CH_3COOH(g) + ~^*$
Dimethyl Ether Pathway	
68	$CH_3^* + CH_3O^* \leftrightarrow H_3C\text{-}OCH_3^* + ~^* \leftrightarrow CH_3OCH_3^* + ~^*$
69	$CH_3OCH_3^* \leftrightarrow CH_3OCH_3(g) + ~^*$

2.3 Microkinetic Modeling

The open-source code CatMAP [28] was used for microkinetic modeling. Initial conditions for the model were 2.5:1 $CH_3OH:O_2$ by mole fraction. The models were run at 0.8 atm pressure and over a range of 10 temperature values from 300 to 1000 K. Gas-phase thermochemistry was described with the ideal gas approximation, and all adsorbate thermochemistry relied on the harmonic approximation. To improve CatMAP's convergence and to avoid numerical stabilities, the initial concentrations of gas-phase species fed to the model are initialized at non-zero values (typically, 0.01 mole fraction). DFT energies and frequencies fed to CatMAP combined BEEF-vdW data from [18] (elementary steps 1-55) with RPBE-D3 data from this work (elementary steps 56-69).

3. Density Functional Theory Results

3.1. Comparison of RPBE, RPBE-D3, and BEEF-vdW Functionals
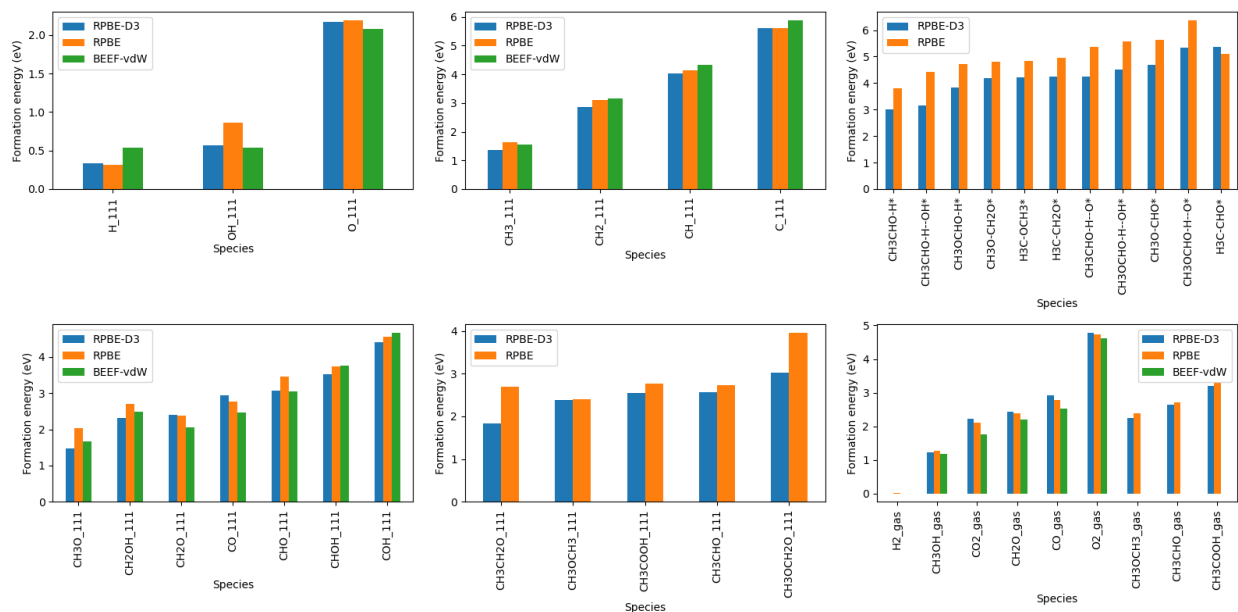
Figure 2. Formation energies for 1) RPBE-optimized, RPBE-D3-evaluated structures (blue, this work), 2) RPBE-optimized, RPBE-evaluated structures (orange, this work), and 3) BEEF-vdW-optimized, BEEF-vdW-evaluated structures (green, [18]*). BEEF-vdW energies are not available for two-carbon compounds.*

The DFT-calculated formation energies were evaluated with the RPBE-D3 GGA functional (including Grimme's DFT-D3 van der Waal corrections with Becke-Jonson damping [19] on structures optimized with the RPBE GGA functional (without van der Waal corrections)). This was done to avoid unphysical compression effects for unconstrained metal atoms in RPBE-D3-optimized metal surfaces. The formation energy $E_{f,gas,i}$ of gas species i was calculated with

$$E_{f,i} = E_{DFT,i} - \sum_j n_j R_j,$$

where the reference R_j are

$$R_H = \frac{1}{2} E_{DFT,H_2}$$

$$R_C = E_{DFT,CH_4} - 4R_H$$

$$R_O = E_{DFT,H_2O} - 2R_H$$

Similarly, the formation energy $E_{f,i}$ of adsorbed species $i@Ag(111)$ was calculated with

$$E_{f,i@Ag(111)} = E_{DFT,i@Ag(111)} - E_{DFT,Ag(111)} - \sum_j n_j R_j$$

Formation energies are presented in Figure 2, which also includes energies calculated by [18] with the BEEF-vdW functional.

The D3 van der Waal corrections on RPBE DFT energies lead to significant differences (~ 0.5 eV) in formation energies for most adsorbates, especially for the larger two-carbon intermediate species CH_3CH_2O and CH_3OCH_2O, which showed very large differences (~1.0 eV) in formation energies. These effects demonstrate the importance of including dispersion correction in the analysis of surface bound intermediates.

Similarly, many of the transition states show significant differences with DFT-D3 van der Waals corrections, with decreases as high as ~1 eV. This implies that van der Waals corrections may have a stabilizing effect on these structures. Because the transition states lie at saddle points on the (RPBE) potential energy surface, energy evaluations with a different (RPBE-D3) potential energy surface are likely to produce significant changes. It is possible that the D3 corrections for transition state formation energies introduce error in activation energy barriers for microkinetic modeling, an effect which may be reduced by using scaling relations. However, the D3-corrected transition state H_3C-CHO formation energy did not show a decrease ($\Delta \cong +0.2$ eV).

For all species, BEEF-vdW energies are largely consistent with RPBE-D3 calculations, especially for adsorbates. Our model combines BEEF-vdW and RPBE-D3 energies, so the lack of major systematic differences in formation energies may reduce the potential inconsistencies of combining functionals. However, it is not standard practice and it should be noted that it is a preliminary model only.

Vibrational frequencies were calculated using the RPBE functional and plotted along with BEEF-vdw vibrational modes from [18] in Figure 3.
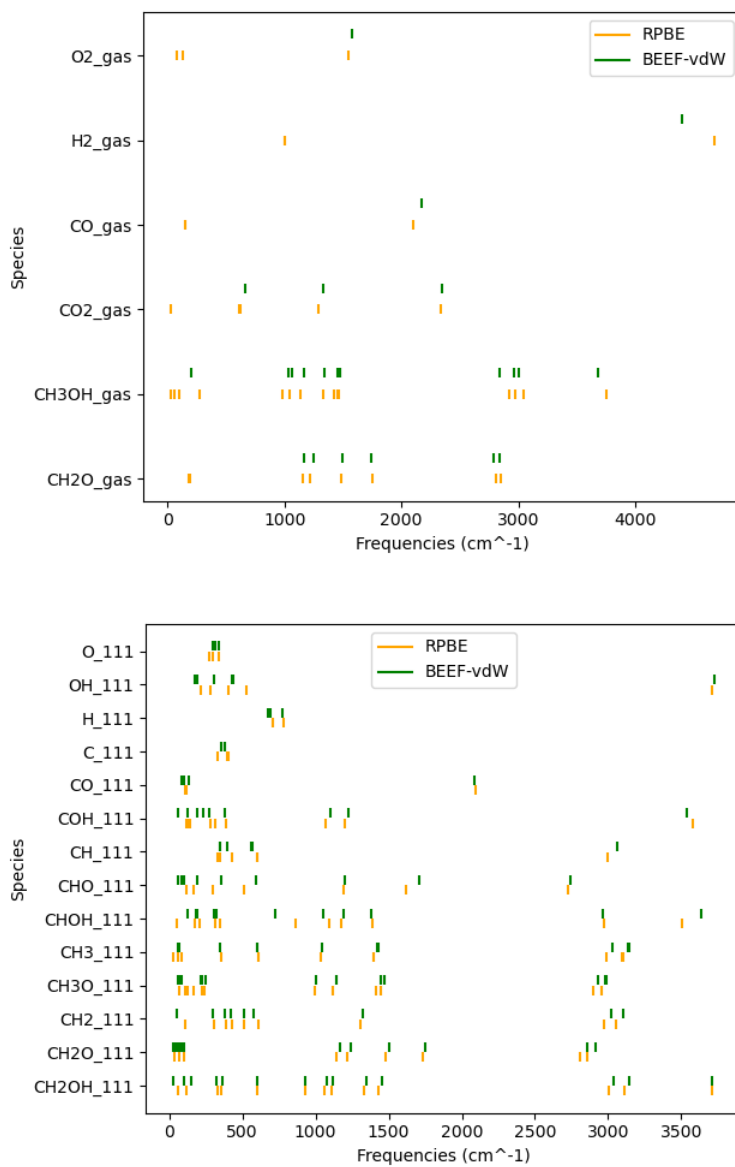
3.2 Elementary Step Activation Barriers

A table of elementary steps, potential energy barriers, reaction potentials, and other thermodynamic information is in the appendix (A.4). Images of initial and final states as well as converged transition states are included in the appendix as well (A.5).

3.2.1 Methanol Adsorption
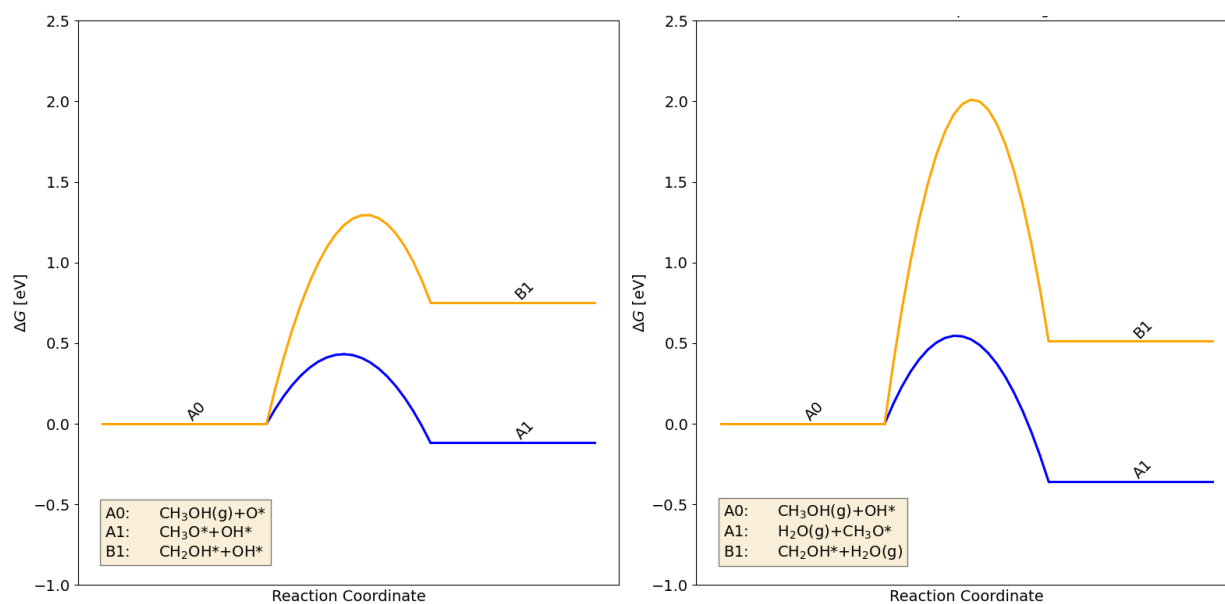
Figure 4. Free energy diagrams of methanol adsorption steps at 600 K.

Formation energies and reaction barriers calculated with DFT (Figure 4) suggest, in agreement with experimental and computational study, that the adsorption of methanol occurs via a dissociative surface oxygen-assisted mechanism. However, the oxidizing species for this step is not O*, as has been suggested before, but instead OH*. In this step, the hydroxyl hydrogen of methanol is transferred to the surface oxygen, forming methoxy. CH_2OH^* may also be formed by

the scission of a C-H bond, though the free-energy diagram shows that CH₂OH* is a less

favorable product than CH₃O*, because of a large activation energy and unfavorable Gibbs free

energy change.

3.2.2 Reaction to Formaldehyde

The subsequent step of formaldehyde synthesis is an additional oxidation step to dehydrogenate

the methoxy intermediate. The dehydrogenation of CH₂OH* is more favorable, by reaction

energies and activation barriers (Table 3), than of CH₃O*, because CH₂OH* is a less stable

intermediate. This creates some competition between these two pathways. While O* reduces the

activation barrier for methoxy dehydrogenation more than OH*, the OH*-assisted pathway has a

more favorable free energy change, creating additional competition that may be temperature-

dependent. The full reaction free energy diagram is shown in Figure 5. Because of CH₃O*'s

favorable energetics in the initial step and experimental evidence supporting its role in the main

synthesis pathway [3], [4], [7], CH₂OH* was neglected in the free energy diagrams for the full

pathway to formaldehyde shown below.

Table 3. Table of free energy changes and barriers for dehydrogenation steps leading to surface formaldehyde at 600 K.

Reaction	$\Delta G_{600\ K}$ (eV)	$\Delta G^{\ddagger}_{600\ K}$ (eV)
$CH_3O^* + O^* \leftrightarrow CH_2O^* + OH^* + *$	-0.36	0.55
$CH_3O^* + OH^* \leftrightarrow CH_2O^* + H_2O + *$	-1.53	0.66
$CH_2OH^* + O^* \leftrightarrow CH_2O^* + OH^*$	0.51	2.01
$CH_2OH^* + OH^* \leftrightarrow CH_2O^* + H_2O + *$	-2.40	0.00
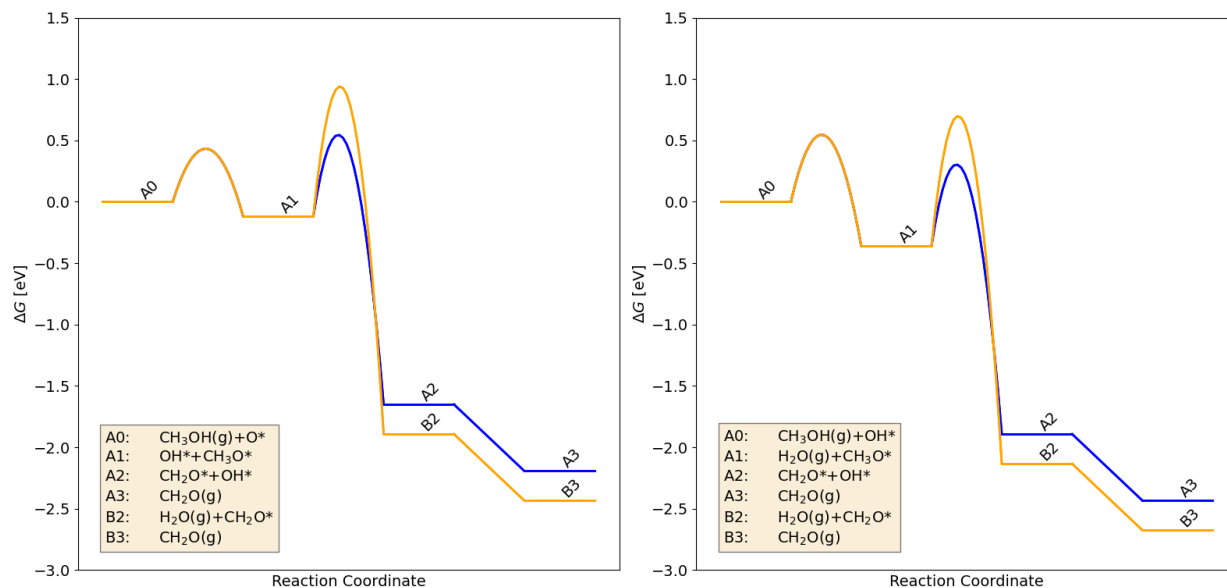
Figure 5. Free energy diagrams for conversion of methanol to formaldehyde at 600 K.

3.2.2 Reaction to Carbon Monoxide and Carbon Dioxide
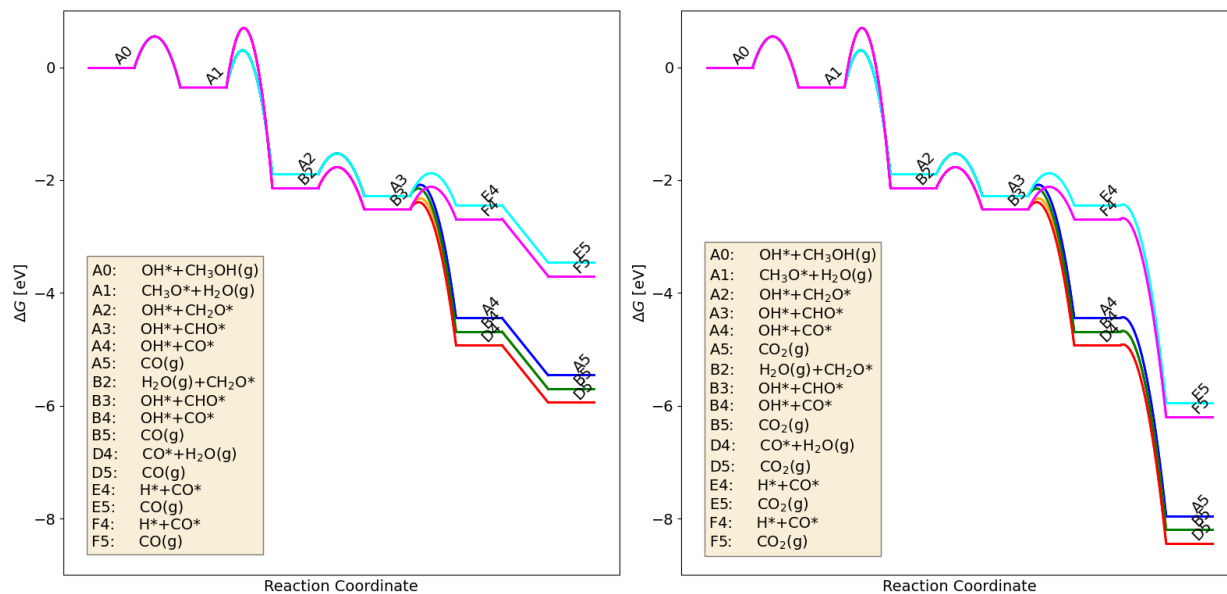
Figure 6. Free energy diagrams for carbon monoxide and carbon dioxide pathways at 600 K.

Desorption of surface formaldehyde is in competition with further oxidation steps that convert surface-bound formaldehyde to carbon monoxide and carbon dioxide. The free energy diagrams in Figure 6 show that pathways through O*-assisted dehydrogenation of the CHO* intermediate

likely lead to formation of both carbon monoxide and carbon dioxide. Carbon dioxide is the favored product at 600 K. As is true for many other steps in the network of elementary reactions, surface-assisted dehydrogenation is not as favorable as those assisted by O* or OH*. As multiple pathways assisted by both O* and OH* show similarly favorable energetics, these species may compete for participation in dehydrogenation mechanisms of the full oxidation scheme.

3.2.3 Acetaldehyde Formation
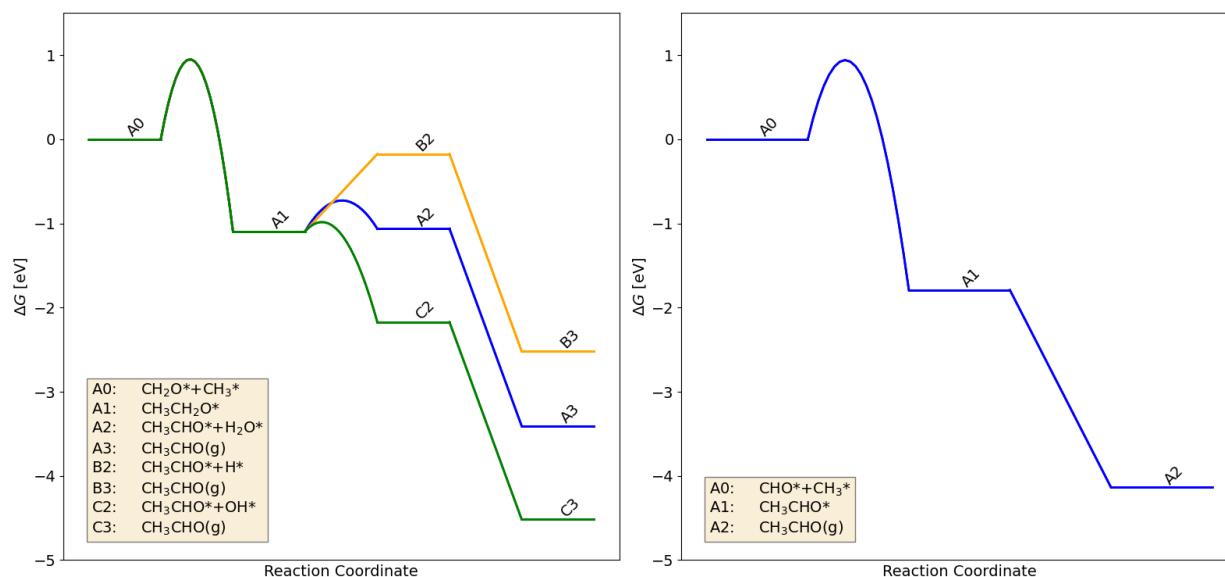
Figure 7. Free energy diagrams of acetaldehyde formation pathways from CH₃ and CH₂O*, and from CH₃* and CHO*.*

DFT energetics for acetaldehyde synthesis pathways are shown in Figure 7. Species geometries used for DFT calculations are shown in Figure 8. Acetaldehyde can be formed from one of two intermediate coupling reactions: 1) CH_3* and CH_2O*, and 2) CH_3* and CHO*. The second intermediate coupling reaction shows better energetics, though it is likely due to the relative instability of the CHO* intermediate. The most favorable pathway for the dehydrogenation of the hemiacetal alcoholate intermediate is through an oxygen-assisted oxidation step. The scheme shows a similar trend to the methyl formate pathway (Figure 9), with an initial intermediate

coupling step and a subsequent dehydrogenation step, though the acetaldehyde pathway faces a larger initial energy barrier for the carbon-carbon coupling reaction. This may explain why methyl formate has been observed for many decades in this reaction and acetaldehyde has only been detected for the first time recently. The barrier for carbon-carbon coupling, however, is accessible at reaction temperatures and the energy pathway for acetaldehyde formation is feasible. Importantly, the activation energies for carbon-carbon coupling reactions are the result of nudged elastic band calculations that are not fully converged and this is a preliminary result only.
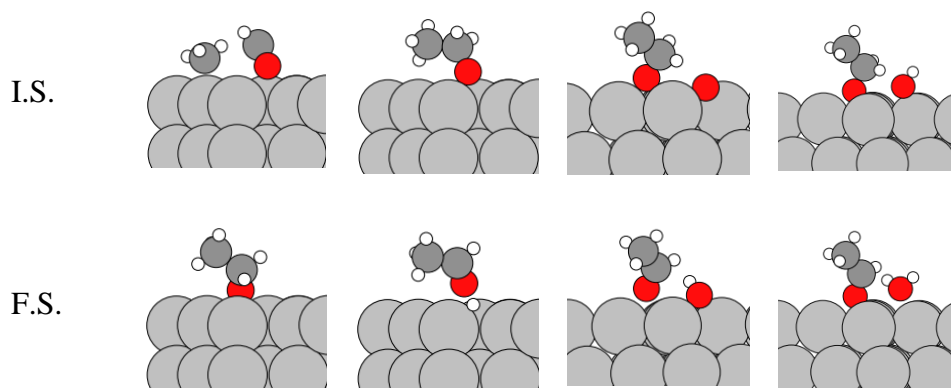
Figure 8. Initial and final structures for reactions, from left to right, CH_3-CH_2O* coupling, surface-assisted dehydrogenation, O*-assisted dehydrogenation, and OH*-assisted dehydrogenation.*

3.2.4 Methyl Formate Synthesis
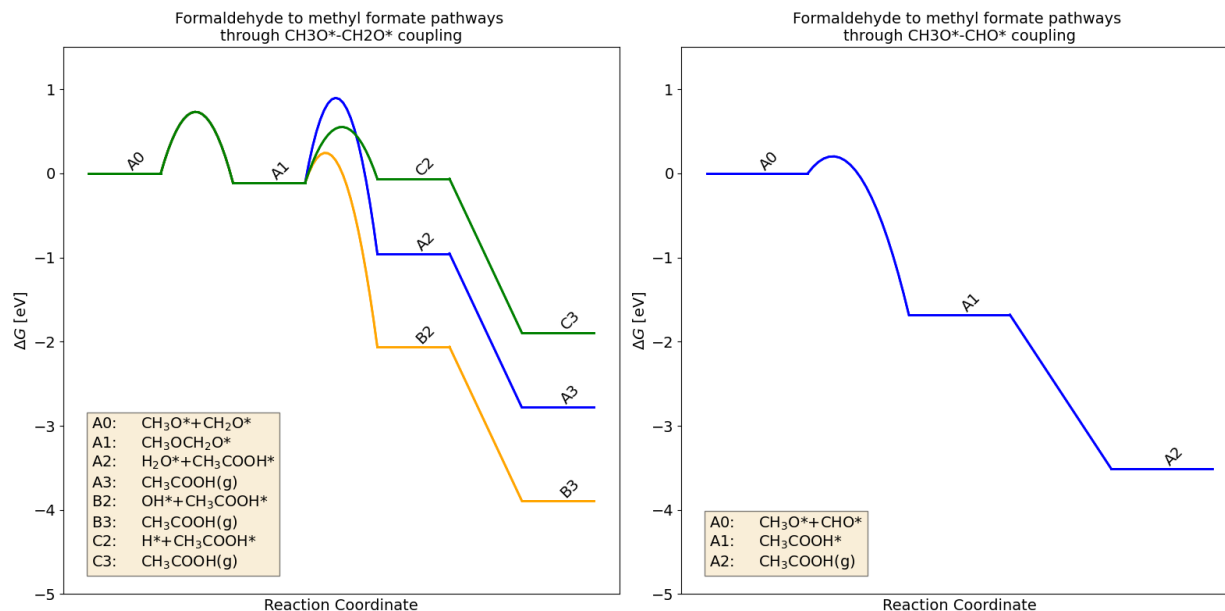
Figure 9. Free energy diagrams for pathways to methyl formate formation from CH_2O^* at 600 K.

DFT energetics for methyl formate synthesis pathways are displayed in Figure 9. Methyl formate can be formed from one of two intermediate coupling reactions: 1) CH_3O^* and CH_2O^*, and 2) CH_3O^* and CHO^*. Just as with acetaldehyde, the second possibility may be more energetically favorable because of its lesser activation energy. This is likely owing to the relative instability of the CHO^* intermediate. Assuming that CHO^* is not less likely to be available for reaction, our calculations support the mechanism hypothesized by Wachs and Madix in [7], where the coupling of methoxy and formaldehyde yields a hemiacetal intermediate, which is then dehydrogenated and desorbed. Specifically, our DFT indicates that dehydrogenation of the $CH_3OCH_2O^*$ intermediate through oxygen is more favorable than through hydroxy or the silver surface.
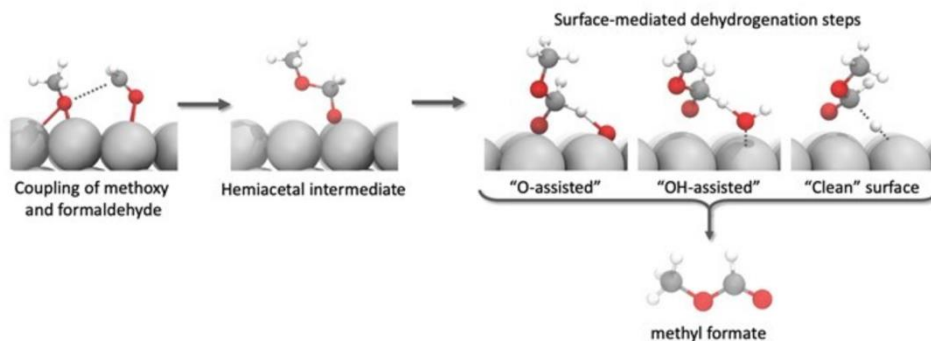
Figure 10. Methoxy-formaldehyde coupling and intermediate dehydrogenation steps.

3.2.5 Further Reaction of Formaldehyde to Dimethyl Ether
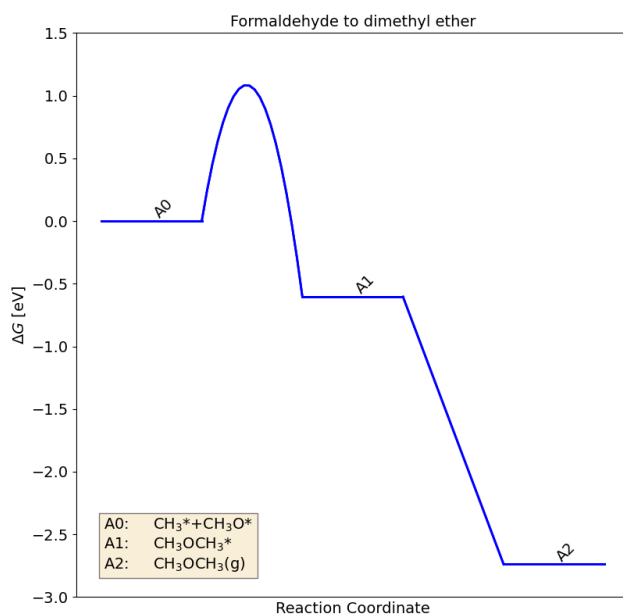
Figure 11. Free energy diagram for conversion of formaldehyde to dimethyl ether.

The model gives only one pathway for the formation of dimethyl ether – a coupling reaction between CH_3^* and CH_3O^*. There is a sizable barrier (~1.0 eV) for this step, though it is accessible at reaction temperatures. The DFT results may then support our mechanism of dimethyl ether formation over silver in trace amounts. Importantly, this activation energy is the result of a nudged elastic band calculation that is not fully converged and this is a preliminary result only.
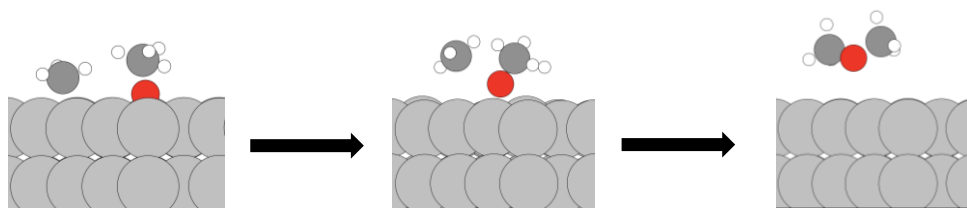
*Figure 12. Structures of initial, transition, and final states in CH₃*-CH₃O* coupling reaction for the dimethyl ether pathway.*

4. Microkinetic Modeling Results
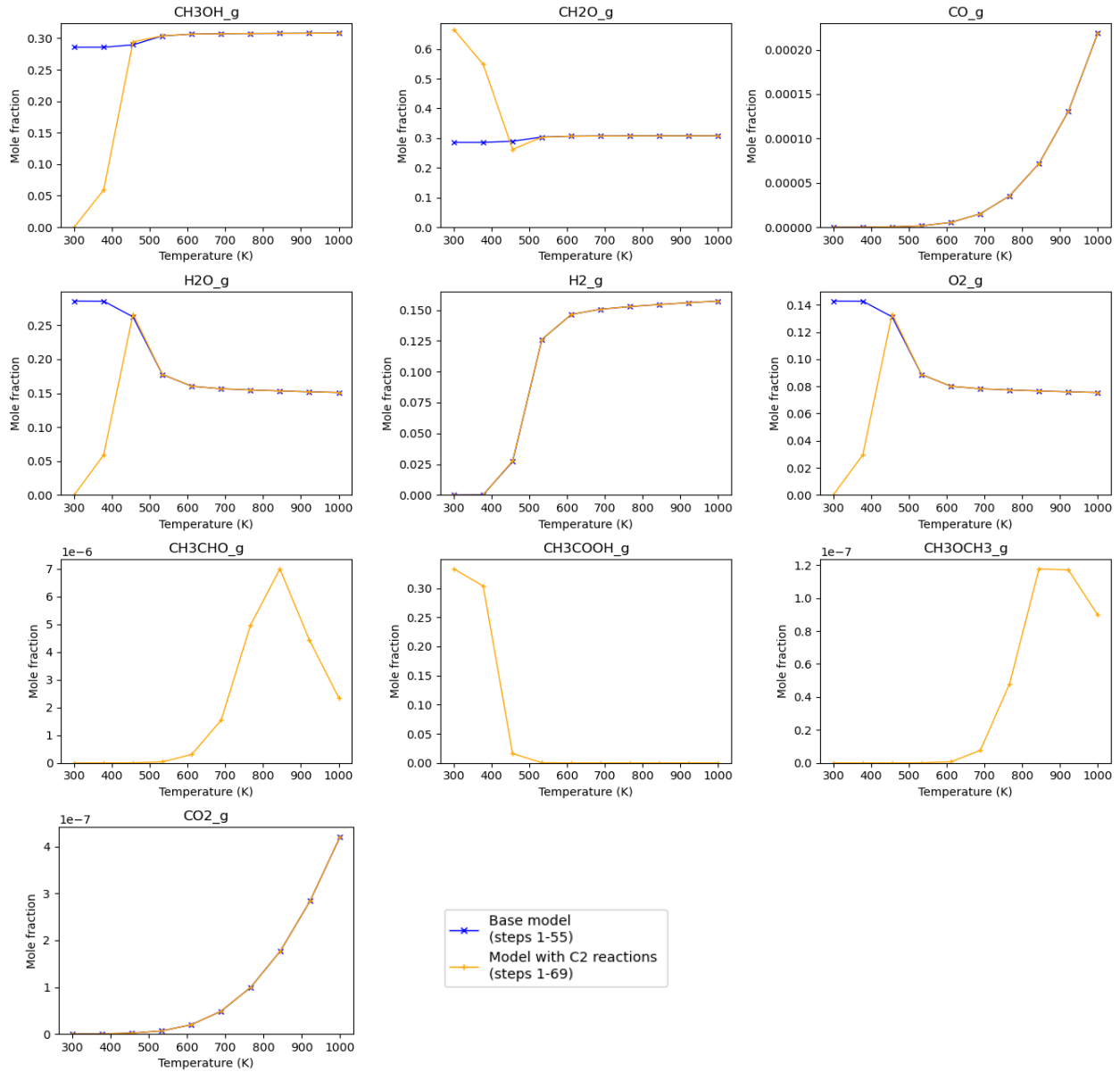
Figure 13. Gas-phase mole fractions from steady-state microkinetic modeling solutions.
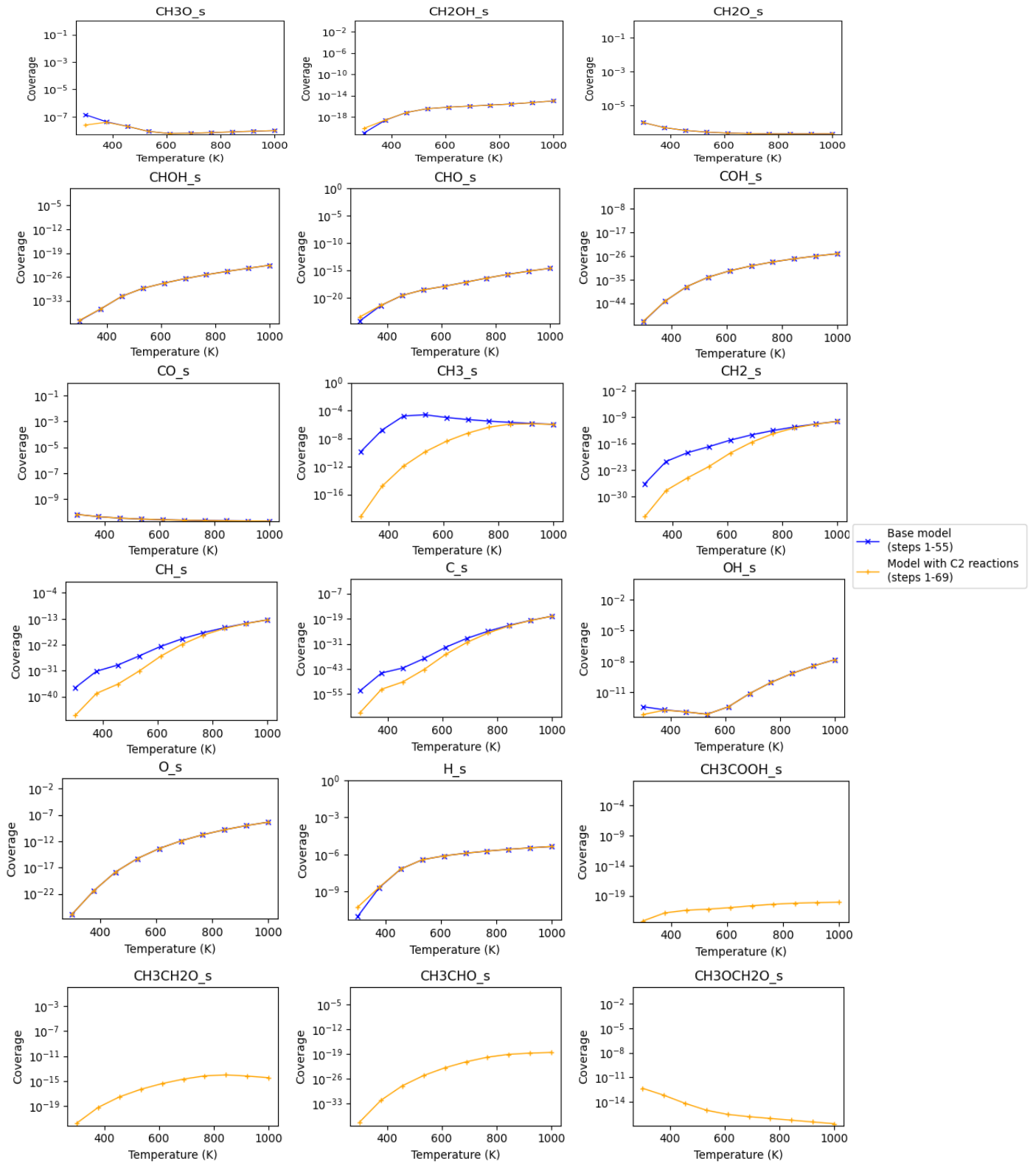
Figure 14. Coverages of surface-bound species from steady-state microkinetic modeling solutions.

Microkinetic models were run for a range of ten temperatures between 300 and 1000 K, at a pressure of 0.8 atm and a feed ratio of 2.5: 1 CH_3OH: O_2. To investigate the effect of including mechanisms for acetaldehyde, methyl formate, and dimethyl ether formation in the reaction scheme, the model was run with and without these additional elementary steps. Below 500 K, the full model gives gas-phase mole fraction results (Figure 13) that show methanol conversion of 100%. Because experiments are generally run at low conversions, correspondence between these results and experimental trends are not expected. They do, however, provide insights into kinetics and validate the additional reaction mechanisms proposed.

Gas-phase mole fraction and surface coverage plots (Figure 14) show that there are significant changes to microkinetic modeling results at lower temperatures due to the addition of the methyl formate formation steps. Below 500 K, which is within the expected range of temperatures characteristic of light-off for formaldehyde synthesis, the full model shows a decrease in methanol, H_2O, and O_2 levels as well as an increase in formaldehyde concentration over the base model. These changes are coincident with high levels of methyl formate production. Coverage results indicate that the full model also shows a depletion of CH_x species and CH_3O on the surface.

At these temperatures, methanol is fully converted to methyl formate and formaldehyde. All gas-phase oxygen is adsorbed to the surface, where it facilitates oxidation steps. All hydrogen species transferred during methanol adsorption or intermediate oxidation steps remain surface-bound as OH* or H*.

The significant depletion of CH_x species on the surface at this kinetic regime is interesting, as neither formaldehyde nor methyl formate pathways involve these species. Barriers for forming these species are mostly quite high and the free energy changes unfavorable. The

higher reaction flux through formaldehyde and methyl formate production pathways likely suppresses flux through these less favorable side reactions, relative to the base model. Lower levels of CH_3O^* are likely due to faster consumption of this intermediate in both main reaction pathways.

Above 500 K, a different kinetic regime for the full model is observed, which corresponds very closely to that of the base model. Methanol is consumed with a conversion of about 50% to formaldehyde product, with trace levels of CO and CO_2. Hydrogen species are desorbed in the form of H_2O or H_2, and O_2 is maintained at a steady-state level of about 8% by mole fraction.

The most abundant surface intermediates are CH_3O^*, CH_2O^*, CO^*, OH^*, and H^* for both models. The abundance of CH_3O^* validates conclusions from DFT free energies that reactions likely proceed through methoxy. The high coverage of OH^* shows how essential nucleophilic surface oxygen is as a participant in dehydrogenation steps.

Acetaldehyde and dimethyl ether concentrations are at low levels, which is consistent with experiment [12] and expected from DFT results showing that these downstream product pathways face large activation energy barriers in intermediate coupling steps. As discussed in the DFT result section, methyl formate and acetaldehyde may be formed directly by coupling reactions involving CHO^*. These coupling reactions are clearly coverage-limited, as this unstable intermediate is only present in trace amounts compared to the competing reactant CH_2O^*. Reaction rates for acetaldehyde and dimethyl ether formation, in addition to facing a larger barrier to intermediate coupling, may also be coverage-limited by CH_3^*, which is also much less abundant than CH_3O^* and CH_2O^*.

The model is preliminary due to it using 1) a combination of functionals in its input data, and 2) three unconverged transition states. Other potential explanations for inconsistencies include the potential for coverage-dependence and adsorbate-adsorbate interaction effects on binding energies. Systematic errors in binding energies may be accounted for with optimization and scaling corrections. Plots of these scaling corrections and their linear fits are in the appendix (A.2).

5. Conclusions and Recommendations for Future Work

A theoretical study on the partial oxidation of methanol and two-carbon species formation over Ag(111) was conducted to improve understanding of reaction mechanisms and energetics. Analysis of literature DFT results show that the most favorable pathways to production of formaldehyde proceed through O^* and OH^*-assisted dehydrogenation steps, in agreement with previous theoretical and experimental results. DFT calculations also give insights into the competing steps that may convert methanol to 1) CH_2O product, 2) more oxidized products CO and CO_2, and 3) products of intermediate coupling reactions such as CH_3OCH_3, CH_3CHO, and CH_3OCHO. These calculations suggest a mechanism for methyl formate formation from the coupling of formaldehyde and methoxy intermediates, followed by an O^*-assisted dehydrogenation reaction. They suggest a similar mechanism for acetaldehyde, where the product of a CH_3^* and CH_2O^* carbon-carbon coupling step is subsequently dehydrogenated by surface oxygen. The methyl formate synthesis mechanism shows more favorable energetics than suggested mechanisms for acetaldehyde and dimethyl ether synthesis pathways, which involve larger activation barriers for initial intermediate coupling steps.

Microkinetic modeling calculations indicated that methyl formate is a favorable product in a full reaction network for methanol partial oxidation systems over silver. Theoretical steady-state solutions to the set of reaction rate equations provide further explanation for experimental results showing greater selectivity to methyl formate than to acetaldehyde or dimethyl ether, due to CH_3^*-coverage-limited reaction steps in the acetaldehyde and dimethyl ether production pathways. Theoretical CHO^* coverages suggest that intermediate coupling steps involving CHO^* are also likely coverage-limited, further supporting DFT evidence that direct mechanisms for methyl formate and acetaldehyde are unlikely.

These theoretical models also provide a basis for further modeling intended to replicate and explain experimental results. This modeling would be able to generate solutions with comparable conversions that correspond more accurately to realistic kinetic regimes. Recent experimental investigations into this reaction have provided a wealth of data that can be used as guides for theoretical DFT and microkinetic modeling research, including *in situ* spatially- and temporally-resolved maps of species concentrations above the silver surface during reaction conditions. Thus, models which include mass-transfer effects and coupled surface- and gas-phase reaction mechanisms may provide greater insights into the workings of methanol partial oxidation and surface catalysis in general. Other products of intermediate coupling reactions on silver and other metals, such as dimethoxy methane and methoxy methanol, have been detected with these new sensing techniques and provide opportunities for more extensive theoretical studies.

Bibliography

[1]   G. J. Millar and M. Collins, "Industrial Production of Formaldehyde Using Polycrystalline Silver Catalyst," *Ind. Eng. Chem. Res.*, vol. 56, no. 33, pp. 9247–9265, 2017, doi: 10.1021/acs.iecr.7b02388.

[2]   S. K. Bhattacharyya, N. K. Nag, and N. D. Ganguly, "Kinetics of vapor-phase oxidation of methanol on reduced silver catalyst," *J. Catal.*, vol. 23, no. 2, pp. 158–167, 1971, doi: 10.1016/0021-9517(71)90037-6.

[3]   D. A. Outka and R. J. Madix, "Brønsted Basicity of Atomic Oxygen on the Au(110) Surface: Reactions with Methanol, Acetylene, Water, and Ethylene," *J. Am. Chem. Soc.*, vol. 109, no. 6, pp. 1708–1714, 1987, doi: 10.1021/ja00240a018.

[4]   J. Wang, X. Xu, J. Deng, Y. Liao, and B. Hong, "In situ Raman spectroscopy studies on the methanol oxidation over silver surface," *Appl. Surf. Sci.*, vol. 120, no. 1–2, pp. 99–105, 1997, doi: 10.1016/S0169-4332(97)00245-6.

[5]   A. C. Van Veen, O. Hinrichsen, and M. Muhler, "Mechanistic studies on the oxidative dehydrogenation of methanol over polycrystalline silver using the temporal-analysis-of-products approach," *J. Catal.*, vol. 210, no. 1, pp. 53–66, 2002, doi: 10.1006/jcat.2002.3682.

[6]   D. A. Robb and P. Harriott, "The kinetics of methanol oxidation on a supported silver catalyst," *J. Catal.*, vol. 35, no. 2, pp. 176–183, Nov. 1974, doi: 10.1016/0021-9517(74)90194-8.

[7]   I. E. Wachs and R. J. Madix, "The oxidation of methanol on a silver (110) catalyst," *Surf. Sci.*, vol. 76, no. 2, pp. 531–558, 1978, doi: 10.1016/0039-6028(78)90113-9.

[8]   M. Qian, M. A. Liauw, and G. Emig, "Formaldehyde synthesis from methanol over silver

catalysts," *Appl. Catal. A Gen.*, vol. 238, no. 2, pp. 211–222, 2003, doi: 10.1016/S0926-860X(02)00340-X.

[9]   A. Nagy, G. Mestl, T. Rühle, G. Weinberg, and R. Schlögl, "The dynamic restructuring of electrolytic silver during the formaldehyde synthesis reaction," *J. Catal.*, vol. 179, no. 2, pp. 548–559, 1998, doi: 10.1006/jcat.1998.2240.

[10]   J. R. H. Lefferts, L., van Ommen, J.G., Ross, "The Oxidative Dehydrogenation of Methanol to Formaldehyde over Silver Catalysts in Relation to the Oxygen-Silver Interaction," *Appl. Catal.*, vol. 23, no. 2, pp. 385–402, 1986.

[11]   G. I. N. Waterhouse, G. A. Bowmaker, and J. B. Metson, "Mechanism and active sites for the partial oxidation of methanol to formaldehyde over an electrolytic silver catalyst," *Appl. Catal. A Gen.*, vol. 265, no. 1, pp. 85–101, 2004, doi: 10.1016/j.apcata.2004.01.016.

[12]   B. Zhou *et al.*, "Near-Surface Imaging of the Multi-Component Gas Phase above a Silver Catalyst During Partial Oxidation of Methanol," *ACS Catal.*, vol. Just Accep, 2020, doi: 10.1021/acscatal.0c04396.

[13]   H. Schubert, U. Tegtmeyer, and R. Schlögl, "On the mechanism of the selective oxidation of methanol over elemental silver," *Catal. Letters*, vol. 28, pp. 383–395, 1994, doi: 10.1007/BF00806069.

[14]   X. Bao, M. Muhler, B. Pettinger, R. Schlögl, and G. Ertl, "On the nature of the active state of silver during catalytic oxidation of methanol," *Catal. Letters*, vol. 22, pp. 215–225, 1993, doi: 10.1007/BF00810368.

[15]   L. Lefferts, J. G. van Ommen, and J. R. H. Ross, "The influence of hydrogen treatment and catalyst morphology on the interaction of oxygen with a silver catalyst," *Appl. Catal.*, vol. 34, pp. 329–339, 1987, doi: 10.1016/S0166-9834(00)82466-5.

[16]   A. Andreasen, H. Lynggaard, C. Stegelmann, and P. Stoltze, "A microkinetic model of the methanol oxidation over silver," *Surf. Sci.*, vol. 544, no. 1, pp. 5–23, 2003, doi: 10.1016/j.susc.2003.08.007.

[17]   A. H. Motagamwala and J. A. Dumesic, "Microkinetic Modeling: A Tool for Rational Catalyst Design," *Chem. Rev.*, 2020, doi: 10.1021/acs.chemrev.0c00394.

[18]   H. Aljama, S. Yoo, J. K. Nørskov, and F. Abild-pedersen, "Methanol Partial Oxidation on Ag (111) from First Principles," *ChemCatChem*, no. 8, pp. 3621–3625, 2016, doi: 10.1002/cctc.201601053.

[19]   S. Grimme, J. Antony, S. Ehrlich, and H. Krieg, "A consistent and accurate ab initio parametrization of density functional dispersion correction (DFT-D) for the 94 elements H-Pu," *J. Chem. Phys.*, vol. 132, no. 15, 2010, doi: 10.1063/1.3382344.

[20]   D. Joubert, "From ultrasoft pseudopotentials to the projector augmented-wave method," *Phys. Rev. B - Condens. Matter Mater. Phys.*, vol. 59, no. 3, pp. 1758–1775, 1999, doi: 10.1103/PhysRevB.59.1758.

[21]   A. Hjorth Larsen *et al.*, "The atomic simulation environment - A Python library for working with atoms," *J. Phys. Condens. Matter*, vol. 29, no. 27, 2017, doi: 10.1088/1361-648X/aa680e.

[22]   G. Kresse and J. Hafner, "Ab initio molecular dynamics for liquid metals," *Phys. Rev. B*, vol. 47, no. 1, pp. 558–561, 1993, doi: 10.1103/PhysRevB.47.558.

[23]   G. Kresse and J. Hafner, "Ab initio molecular-dynamics simulation of the liquid-metalamorphous- semiconductor transition in germanium," *Phys. Rev. B*, vol. 49, no. 20, pp. 14251–14269, 1994, doi: 10.1103/PhysRevB.49.14251.

[24]   G. Kresse and J. Furthmüller, "Efficiency of ab-initio total energy calculations for metals

and semiconductors using a plane-wave basis set," *Comput. Mater. Sci.*, vol. 6, no. 1, pp. 15–50, 1996, doi: 10.1016/0927-0256(96)00008-0.

[25]   J. Kresse, G., Furthmüller, "Efficient iterative schemes for ab initio total-energy calculations using a plane-wave basis set," *Phys. Rev. B*, vol. 54, no. 16, pp. 169–186, 1996.

[26]   S. Mallikarjun Sharada, R. K. B. Karlsson, Y. Maimaiti, J. Voss, and T. Bligaard, "Adsorption on transition metal surfaces: Transferability and accuracy of DFT using the ADS41 dataset," *Phys. Rev. B*, vol. 100, no. 3, 2019, doi: 10.1103/physrevb.100.035439.

[27]   P. Janthon, S. M. Kozlov, F. Vin, J. Limtrakul, and F. Illas, "Establishing the Accuracy of Broadly Used Density Functionals in Describing Bulk Properties of Transition Metals," 2013, doi: 10.1021/ct3010326.

[28]   A. J. Medford *et al.*, "CatMAP: A Software Package for Descriptor-Based Microkinetic Mapping of Catalytic Trends," *Catal. Letters*, vol. 145, no. 3, pp. 794–807, 2015, doi: 10.1007/s10562-015-1495-6.

<center>**Appendix**</center>

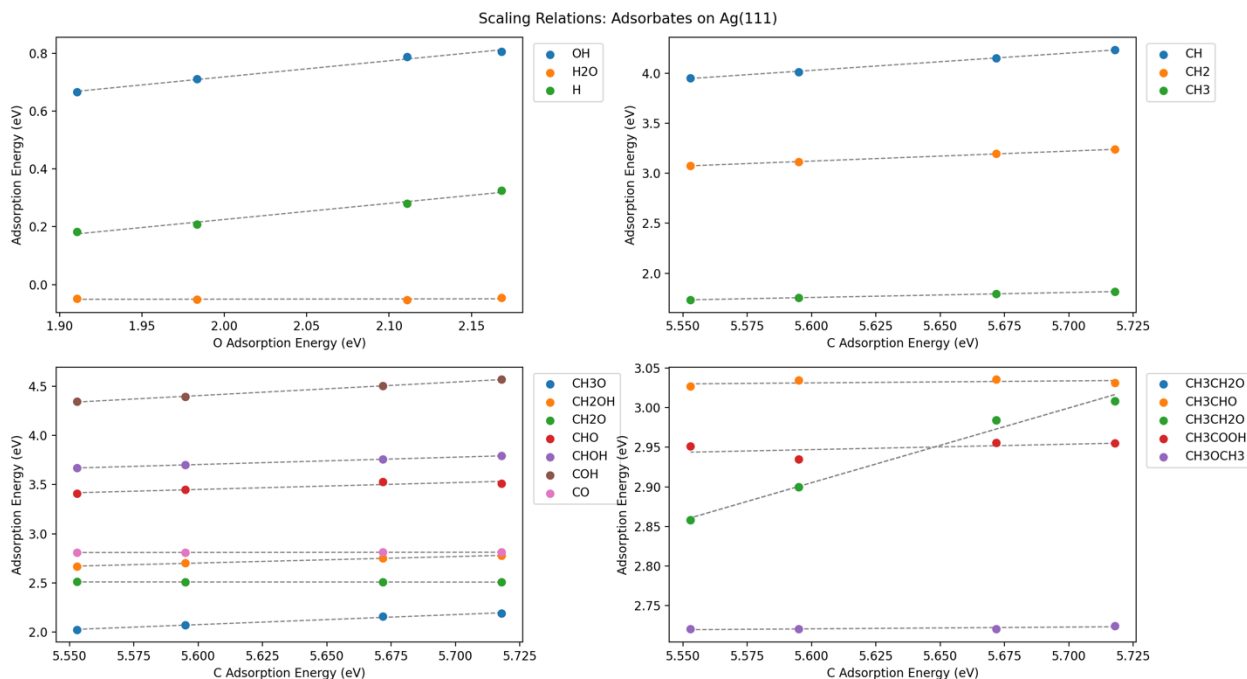## A1. Convergence Tests
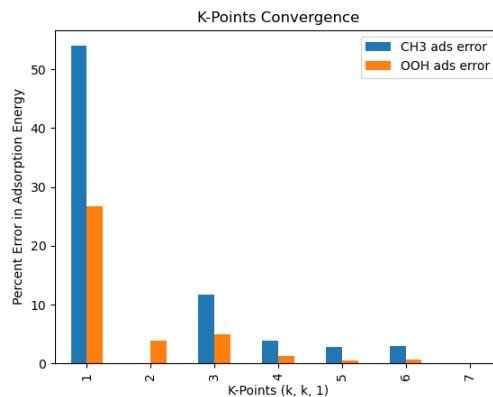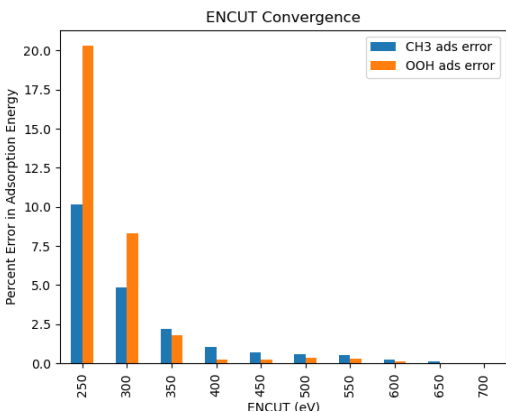
A2. Scaling Relations

Scaling relations were constructed by running binding energy calculations on silver lattices with changes in lattice spacing of -5, -2.5, 0, 2.5, and 5%. DFT methods from methodology section apply.

A3. Silver-Oxygen Phase Calculations

Each oxygen phase, O_α, O_β, and O_γ, was constructed with ASE and underwent a geometry

optimization. DFT methods from methodology section apply.
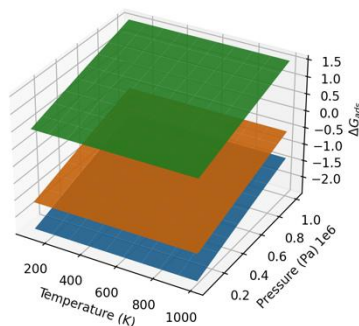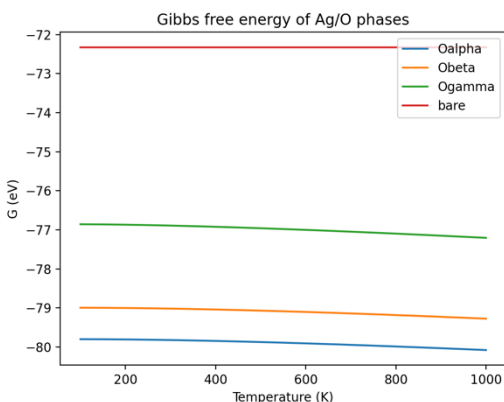
A4. Elementary Step Thermochemistry

BEEF-vdW DFT energies are italicized. Non-italicized DFT energies are RPBE-D3. Energy

barriers from nudged elastic bands that are not converged to within -.05 eV/Å at 500 eV and (4,

4, 1) gamma-centered k-points include an asterisk (*). Error in transition state energy and

vibrations for these steps are propagated through the other thermodynamic barriers and have

asterisks also.

	Reaction	ΔE_{DFT} (eV)	$\Delta E^{\ddagger}_{DFT}$ (eV)	$\Delta G_{300\,K}$ (eV)	$\Delta G^{\ddagger}_{300\,K}$ (eV)	$\Delta H_{300\,K}$ (eV)	$\Delta H^{\ddagger}_{300\,K}$ (eV)	$\Delta S_{300\,K}$ (eV/K)	$\Delta S^{\ddagger}_{300\,K}$ (eV/K)
1	$CH_3OH + O^* + * \leftrightarrow CH_3O^* + OH^*$	*0.65*	*0.65*	*-0.80*	*0.00*	*1.83*	*1.83*	*0.99*	*0.99*
2	$CH_3OH + OH^* + * \leftrightarrow CH_3O^* + H_2O + *$	*-1.06*	*0.00*	*-0.57*	*0.00*	*-2.39*	*0.00*	*-0.46*	*0.00*
3	$CH_3O^* + O^* \leftrightarrow CH_2O^* + OH^* + *$	*-0.06*	*0.00*	*-0.21*	*0.07*	*-0.81*	*0.00*	*0.16*	*0.16*
4	$CH_3O^* + OH^* \leftrightarrow CH_2O^* + H_2O + * + *$	*-1.15*	*0.74*	*-1.35*	*0.61*	*-1.10*	*0.72*	*0.17*	*0.17*
5	$CH_3OH + O^* + * \leftrightarrow CH_2OH^* + OH^*$	*-0.15*	*1.18*	*-0.99*	*1.03*	*0.47*	*1.16*	*0.79*	*0.79*
6	$CH_3OH + OH^* + * \leftrightarrow CH_2OH^* + H_2O + *$	*-0.23*	*0.46*	*0.26*	*0.82*	*-1.58*	*0.00*	*-0.49*	*0.00*

7	$CH_2OH^* + O^* \leftrightarrow CH_2O^* + OH^*$	0.77	1.25	0.62	1.58	-0.01	0.00	0.13	0.13
8	$CH_2OH^* + OH^* \leftrightarrow CH_2O^* + H_2O + *$	-1.98	0.00	-2.19	0.00	-1.91	0.01	0.20	0.20
9	$CH_2OH^* + O^* \leftrightarrow CHOH^* + OH^*$	-0.98	0.14	-1.83	0.07	-0.33	0.16	0.82	0.82
10	$CH_2OH^* + OH^* \leftrightarrow CHOH^* + H_2O + *$	-0.26	0.59	-0.30	0.38	-0.25	0.61	-0.02	0.06
11	$CHOH^* + O^* \leftrightarrow CHO^* + OH^*$	0.74	0.79	0.06	0.64	1.33	1.33	0.61	0.61
12	$CHOH^* + OH^* \leftrightarrow CHO^* + H_2O + *$	-2.26	0.00	-2.37	0.00	-2.21	0.00	0.11	0.11
13	$CHOH^* + O^* \leftrightarrow COH^* + OH^*$	-1.26	0.00	-2.01	0.00	-0.64	0.00	0.73	0.73
14	$CHOH^* + OH^* \leftrightarrow COH^* + H_2O + *$	-0.64	0.25	-0.74	0.09	-0.60	0.27	0.10	0.10
15	$COH^* + O^* \leftrightarrow CO^* + OH^*$	0.36	0.69	-0.38	0.52	0.97	0.97	0.72	0.72
16	$COH^* + OH^* \leftrightarrow CO^* + H_2O + *$	-3.73	0.00	-3.78	0.00	-3.72	0.00	0.04	0.04
17	$CH_2O^* + O^* \leftrightarrow CHO^* + OH^*$	-2.73	0.00	-3.41	0.00	-2.14	0.00	0.66	0.66
18	$CH_2O^* + OH^* \leftrightarrow CHO^* + H_2O + *$	-0.54	0.36	-0.48	0.27	-0.55	0.34	-0.10	0.00
19	$CHO^* + O^* \leftrightarrow CO^* + OH^*$	0.46	0.93	-0.12	0.90	1.02	1.02	0.52	0.52
20	$CHO^* + OH^* \leftrightarrow CO^* + H_2O + *$	-2.12	0.11	-2.14	0.13	-2.10	0.10	0.03	0.03
21	$CH_3OH + * + * \leftrightarrow CH_3O^* + H^*$	-1.12	0.00	-1.78	0.00	-0.53	0.00	0.65	0.65
22	$CH_3OH + * + * \leftrightarrow CH_2OH^* + H^*$	1.02	1.59	1.39	1.88	-0.33	0.25	-0.50	0.00
23	$CH_3OH + * + * \leftrightarrow CH_3 + OH^*$	1.84	2.51	2.22	2.78	0.48	1.18	-0.53	0.00
24	$CH_3O^* + * \leftrightarrow CH_2O + H^*$	0.90	1.92	1.32	2.28	-0.44	0.58	-0.50	0.00
25	$CH_3O^* + * \leftrightarrow CH_3^* + O^*$	0.92	1.21	0.61	1.02	0.96	1.20	0.13	0.13
26	$CH_2O^* \leftrightarrow CH_2O^* \leftrightarrow CH_2O + *$	1.96	2.54	1.89	2.45	1.95	2.53	-0.04	0.00
27	$CH_2O^* + * \leftrightarrow CHO^* + H^*$	0.15	0.15	-0.23	0.00	0.82	0.82	0.33	0.33
28	$CH_2O^* + * \leftrightarrow CH_2^* + O^*$	1.54	1.81	1.48	1.70	1.51	1.78	-0.14	0.00
29	$CHO^* + * \leftrightarrow CO^* + H^*$	3.20	3.75	3.27	3.83	3.16	3.70	-0.18	0.00
30	$CHO^* + * \leftrightarrow CH^* + O^*$	-0.04	0.58	-0.18	0.40	-0.05	0.59	-0.01	0.00
31	$CH_2OH^* + * \leftrightarrow CH_2O^* + H^*$	3.36	3.74	3.38	3.75	3.34	3.71	-0.09	0.00
32	$CH_2OH^* + * \leftrightarrow CHOH^* + H^*$	0.10	1.07	-0.23	0.78	0.15	1.11	0.16	0.16
33	$CH_2OH^* + * \leftrightarrow CH_2^* + OH^*$	1.81	1.92	1.66	1.68	1.81	1.93	-0.05	0.04
34	$CHOH^* + * \leftrightarrow COH^* + H^*$	1.22	1.78	1.08	1.64	1.25	1.79	0.02	0.02
35	$CHOH^* + * \leftrightarrow CHO^* + H^*$	1.43	1.72	1.22	1.52	1.46	1.72	0.06	0.06
36	$CHOH^* + * \leftrightarrow CH^* + OH^*$	-0.18	0.53	-0.41	0.31	-0.15	0.54	0.07	0.07
37	$COH^* + * \leftrightarrow CO^* + H^*$	1.11	1.71	1.02	1.60	1.13	1.73	0.02	0.02
38	$COH^* + * \leftrightarrow C^* + OH^*$	-1.65	0.64	-1.81	0.53	-1.66	0.64	0.00	0.04

39	$CH_3^* + * \leftrightarrow CH_2^* + H^*$	*1.77*	*2.43*	*1.76*	*2.38*	*1.76*	*2.42*	*-0.04*	*0.00*
40	$CH_2^* + * \leftrightarrow CH^* + H^*$	*2.16*	*2.42*	*1.99*	*2.24*	*2.17*	*2.42*	*-0.01*	*0.00*
41	$CH^* + * \leftrightarrow C^* + H^*$	*1.70*	*1.98*	*1.60*	*1.85*	*1.69*	*1.96*	*-0.05*	*0.00*
42	$CH_3^* + O^* \leftrightarrow CH_2^* + OH^*$	*2.09*	*2.48*	*1.96*	*2.32*	*2.09*	*2.48*	*0.00*	*0.00*
43	$CH_2^* + O^* \leftrightarrow CH^* + OH^*$	*0.08*	*0.98*	*0.03*	*0.81*	*0.11*	*0.98*	*0.03*	*0.03*
44	$CH^* + O^* \leftrightarrow C^* + OH^*$	*-0.37*	*0.76*	*-0.36*	*0.65*	*-0.37*	*0.75*	*-0.02*	*0.00*
45	$CH_3^* + OH^* \leftrightarrow CH_2^* + * + H_2O$	*0.01*	*1.19*	*0.00*	*1.05*	*0.03*	*1.19*	*0.03*	*0.03*
46	$CH_2^* + OH^* \leftrightarrow CH^* + * + H_2O$	*1.08*	*1.17*	*0.39*	*1.00*	*1.68*	*1.68*	*0.65*	*0.65*
47	$CH^* + OH^* \leftrightarrow C^* + * + H_2O$	*0.63*	*0.85*	*0.00*	*0.73*	*1.20*	*1.20*	*0.61*	*0.61*
48	$CO + * \leftrightarrow CO^*$	*1.01*	*1.25*	*0.36*	*1.08*	*1.60*	*1.60*	*0.66*	*0.66*
49	$CO_2 + * + * \leftrightarrow CO^* + O^*$	*-0.06*	*0.00*	*0.48*	*0.48*	*-0.21*	*0.00*	*-0.53*	*0.00*
50	$CO^* + * \leftrightarrow C^* + O^*$	*2.81*	*2.81*	*3.14*	*3.14*	*2.54*	*2.54*	*-0.38*	*0.00*
51	$H_2O + * + * \leftrightarrow OH^* + H^*$	*5.49*	*5.96*	*5.53*	*5.97*	*5.47*	*5.94*	*-0.08*	*0.00*
52	$OH^* + * \leftrightarrow O^* + H^*$	*1.08*	*1.74*	*1.60*	*2.16*	*0.48*	*1.16*	*-0.66*	*0.00*
53	$O_2 + * + * \leftrightarrow O^* + O^*$	*2.08*	*2.70*	*1.96*	*2.52*	*2.06*	*2.68*	*-0.04*	*0.00*
54	$H_2 + * + * \leftrightarrow H^* + H^*$	*-0.41*	*1.11*	*0.11*	*1.57*	*-0.54*	*1.00*	*-0.50*	*0.00*
55	$OH^* + OH^* \leftrightarrow H_2O + O^* + *$	*1.07*	*1.78*	*1.55*	*2.18*	*0.73*	*1.44*	*-0.56*	*0.00*
56	$CH_3^* + CH_3O^* \leftrightarrow CH_3OCH_3^* + *$	1.00	1.00	0.36	0.55	1.58	1.58	0.62	0.62
57	$CH_3OCH_3^* \leftrightarrow CH_3OCH_3(g) + *$	-0.82	1.02	-0.67	1.02	-0.85	1.00	-0.05	0.00
58	$CH_3CH_2O^* + OH^* \leftrightarrow CH_3CHO^* + H_2O^*$	-0.13	0.00	-1.30	0.00	1.64	1.64	0.82	0.82
59	$CH_3CH_2O^* + * \leftrightarrow CH_3CHO^* + H^*$	0.36	0.78	0.18	0.52	0.40	0.82	0.16	0.16
60	$CH_3CH_2O^* + O^* \leftrightarrow CH_3CHO^* + OH^*$	1.27	1.27	0.99	0.99	1.27	1.27	0.07	0.07
61	$CH_3^* + CH_2O^* \leftrightarrow CH_3CH_2O^* + *$	-0.81	0.34*	-0.97	0.18*	-0.79	0.36*	0.11	0.11*
62	$CH_3^* + CHO^* \leftrightarrow CH_3CHO^* + *$	-1.76	0.64*	-1.41	0.78*	-1.85	0.60*	-0.29	0.00*
63	$CH_3CHO^* \leftrightarrow CH_3CHO(g) + *$	-2.03	0.78	-1.90	0.79	-2.08	0.73	-0.08	0.00
64	$CH_3OCH_2O^* + OH^* \leftrightarrow CH_3COOH^* + H_2O$	0.08	0.08	-1.34	0.00	1.09	1.09	0.96	0.96
65	$CH_3OCH_2O^* + O^* \leftrightarrow CH_3COOH^* + OH^*$	-0.84	0.94*	-0.84	0.87*	-0.84	0.90	0.01	0.01*
66	$CH_3OCH_2O^* + * \leftrightarrow CH_3COOH^* + H^*$	-2.02	0.23	-1.99	0.29	-2.02	0.22	-0.04	0.00
67	$CH_3O^* + CH_2O^* \leftrightarrow CH_3OCH_2O^* + *$	0.06	0.82	-0.03	0.65	0.04	0.82	-0.08	0.00
68	$CH_3O^* + CHO^* \leftrightarrow CH_3COOH^* + *$	-0.68	0.47	-0.42	0.57	-0.79	0.43	-0.27	0.00

69	$CH_3COOH^* \leftrightarrow CH_3COOH(g) + ^*$	-2.16	0.00	-1.93	0.02	-2.26	0.00	-0.21	0.00

	Reaction	ΔE_{DFT} (eV)	$\Delta E_{DFT}^{\ddagger}$ (eV)	$\Delta G_{600\,K}$ (eV	$\Delta G_{600\,K}^{\ddagger}$ (eV)	$\Delta H_{600\,K}$ (eV)	$\Delta H_{600\,K}^{\ddagger}$ (eV)	$\Delta S_{600\,K}$ (eV/K)	$\Delta S_{600\,K}^{\ddagger}$ (eV/K)
1	$CH_3OH + O^* + ^* \leftrightarrow CH_3O^* + OH^*$	0.65	0.65	-1.83	0.00	1.92	1.92	2.11	2.11
2	$CH_3OH + OH^* + ^* \leftrightarrow CH_3O^* + H_2O + ^*$	-1.06	0.00	-0.12	0.43	-2.32	0.00	-0.83	0.00
3	$CH_3O^* + O^* \leftrightarrow CH_2O^* + OH^* + ^*$	-0.06	0.00	-0.36	0.55	-0.80	0.00	0.34	0.34
4	$CH_3O^* + OH^* \leftrightarrow CH_2O^* + H_2O + ^* + ^*$	-1.15	0.74	-1.53	0.66	-1.08	0.72	0.37	0.37
5	$CH_3OH + O^* + ^* \leftrightarrow CH_2OH^* + OH^*$	-0.15	1.18	-1.77	1.06	0.45	1.15	1.54	1.54
6	$CH_3OH + OH^* + ^* \leftrightarrow CH_2OH^* + H_2O + ^*$	-0.23	0.46	0.75	1.30	-1.52	0.00	-0.92	0.00
7	$CH_2OH^* + O^* \leftrightarrow CH_2O^* + OH^*$	0.77	1.25	0.51	2.01	0.00	0.00	0.25	0.25
8	$CH_2OH^* + OH^* \leftrightarrow CH_2O^* + H_2O + ^*$	-1.98	0.00	-2.40	0.00	-1.87	0.01	0.46	0.46
9	$CH_2OH^* + O^* \leftrightarrow CHOH^* + OH^*$	-0.98	0.14	-2.65	0.02	-0.35	0.16	1.62	1.62
10	$CH_2OH^* + OH^* \leftrightarrow CHOH^* + H_2O + ^*$	-0.26	0.59	-0.29	0.32	-0.23	0.62	0.00	0.14
11	$CHOH^* + O^* \leftrightarrow CHO^* + OH^*$	0.74	0.79	-0.53	0.60	1.30	1.30	1.17	1.17
12	$CHOH^* + OH^* \leftrightarrow CHO^* + H_2O + ^*$	-2.26	0.00	-2.50	0.00	-2.18	0.00	0.28	0.28
13	$CHOH^* + O^* \leftrightarrow COH^* + OH^*$	-1.26	0.00	-2.74	0.00	-0.65	0.00	1.44	1.44
14	$CHOH^* + OH^* \leftrightarrow COH^* + H_2O + ^*$	-0.64	0.25	-0.85	0.04	-0.55	0.28	0.26	0.26
15	$COH^* + O^* \leftrightarrow CO^* + OH^*$	0.36	0.69	-1.09	0.45	0.97	0.97	1.43	1.43
16	$COH^* + OH^* \leftrightarrow CO^* + H_2O + ^*$	-3.73	0.00	-3.81	0.00	-3.73	0.00	0.06	0.06
17	$CH_2O^* + O^* \leftrightarrow CHO^* + OH^*$	-2.73	0.00	-4.05	0.00	-2.21	0.00	1.23	1.23
18	$CH_2O^* + OH^* \leftrightarrow CHO^* + H_2O + ^*$	-0.54	0.36	-0.38	0.36	-0.53	0.33	-0.18	0.00
19	$CHO^* + O^* \leftrightarrow CO^* + OH^*$	0.46	0.93	-0.62	1.05	0.99	0.99	0.99	0.99
20	$CHO^* + OH^* \leftrightarrow CO^* + H_2O + ^*$	-2.12	0.11	-2.17	0.19	-2.11	0.07	0.05	0.05
21	$CH_3OH + ^* + ^* \leftrightarrow CH_3O^* + H^*$	-1.12	0.00	-2.41	0.13	-0.59	0.00	1.21	1.21
22	$CH_3OH + ^* + ^* \leftrightarrow CH_2OH^* + H^*$	1.02	1.59	1.88	2.36	-0.26	0.31	-0.90	0.00
23	$CH_3OH + ^* + ^* \leftrightarrow CH_3 + OH^*$	1.84	2.51	2.75	3.21	0.54	1.26	-0.99	0.00
24	$CH_3O^* + ^* \leftrightarrow CH_2O + H^*$	0.90	1.92	1.81	2.75	-0.36	0.64	-0.90	0.00
25	$CH_3O^* + ^* \leftrightarrow CH_3^* + O^*$	0.92	1.21	0.46	1.04	0.99	1.21	0.30	0.30

26	$CH_2O^* \leftrightarrow CH_2O^* \leftrightarrow CH_2O + *$	1.96	2.54	1.93	2.48	1.96	2.54	-0.07	0.00
27	$CH_2O^* + * \leftrightarrow CHO^* + H^*$	0.15	0.15	-0.54	0.00	0.77	0.77	0.58	0.58
28	$CH_2O^* + * \leftrightarrow CH_2^* + O^*$	1.54	1.81	1.62	1.82	1.53	1.79	-0.25	0.00
29	$CHO^* + * \leftrightarrow CO^* + H^*$	3.20	3.75	3.44	4.04	3.19	3.70	-0.32	0.00
30	$CHO^* + * \leftrightarrow CH^* + O^*$	-0.04	0.58	-0.17	0.40	-0.05	0.60	-0.03	0.02
31	$CH_2OH^* + * \leftrightarrow CH_2O^* + H^*$	3.36	3.74	3.47	3.85	3.36	3.71	-0.15	0.00
32	$CH_2OH^* + * \leftrightarrow CHOH^* + H^*$	0.10	1.07	-0.41	0.69	0.19	1.14	0.39	0.39
33	$CH_2OH^* + * \leftrightarrow CH_2^* + OH^*$	1.81	1.92	1.71	1.71	1.84	1.96	-0.07	0.12
34	$CHOH^* + * \leftrightarrow COH^* + H^*$	1.22	1.78	1.03	1.63	1.32	1.84	0.14	0.14
35	$CHOH^* + * \leftrightarrow CHO^* + H^*$	1.43	1.72	1.14	1.53	1.51	1.73	0.19	0.19
36	$CHOH^* + * \leftrightarrow CH^* + OH^*$	-0.18	0.53	-0.50	0.26	-0.11	0.56	0.21	0.21
37	$COH^* + * \leftrightarrow CO^* + H^*$	1.11	1.71	0.97	1.56	1.19	1.76	0.12	0.12
38	$COH^* + * \leftrightarrow C^* + OH^*$	-1.65	0.64	-1.81	0.50	-1.67	0.62	-0.01	0.05
39	$CH_3^* + * \leftrightarrow CH_2^* + H^*$	1.77	2.43	1.79	2.42	1.78	2.42	-0.06	0.00
40	$CH_2^* + * \leftrightarrow CH^* + H^*$	2.16	2.42	1.98	2.25	2.22	2.45	0.06	0.06
41	$CH^* + * \leftrightarrow C^* + H^*$	1.70	1.98	1.64	1.91	1.70	1.96	-0.08	0.00
42	$CH_3^* + O^* \leftrightarrow CH_2^* + OH^*$	2.09	2.48	1.96	2.32	2.10	2.47	0.01	0.01
43	$CH_2^* + O^* \leftrightarrow CH^* + OH^*$	0.08	0.98	-0.02	0.80	0.16	1.00	0.13	0.13
44	$CH^* + O^* \leftrightarrow C^* + OH^*$	-0.37	0.76	-0.35	0.70	-0.36	0.73	-0.01	0.00
45	$CH_3^* + OH^* \leftrightarrow CH_2^* + * + H_2O$	0.01	1.19	-0.03	1.04	0.03	1.17	0.08	0.08
46	$CH_2^* + OH^* \leftrightarrow CH^* + * + H_2O$	1.08	1.17	-0.26	0.97	1.68	1.68	1.29	1.29
47	$CH^* + OH^* \leftrightarrow C^* + * + H_2O$	0.63	0.85	-0.59	0.76	1.16	1.16	1.16	1.16
48	$CO + * \leftrightarrow CO^*$	1.01	1.25	-0.27	1.04	1.56	1.56	1.25	1.25
49	$CO_2 + * + * \leftrightarrow CO^* + O^*$	-0.06	0.00	1.01	1.01	-0.20	0.00	-1.05	0.00
50	$CO^* + * \leftrightarrow C^* + O^*$	2.81	2.81	3.51	3.52	2.59	2.59	-0.70	0.00
51	$H_2O + * + * \leftrightarrow OH^* + H^*$	5.49	5.96	5.60	6.06	5.51	5.95	-0.12	0.00
52	$OH^* + * \leftrightarrow O^* + H^*$	1.08	1.74	2.24	2.76	0.54	1.21	-1.24	0.00
53	$O_2 + * + * \leftrightarrow O^* + O^*$	2.08	2.70	2.00	2.55	2.06	2.67	-0.07	0.00
54	$H_2 + * + * \leftrightarrow H^* + H^*$	-0.41	1.11	0.66	2.09	-0.46	1.06	-0.94	0.00
55	$OH^* + OH^* \leftrightarrow H_2O + O^* + *$	1.07	1.78	2.12	2.73	0.73	1.45	-1.12	0.00
56	$CH_3^* + CH_3O^* \leftrightarrow CH_3OCH_3^* + *$	1.00	1.00	-0.24	0.61	1.52	1.52	1.17	1.17
57	$CH_3OCH_3^* \leftrightarrow CH_3OCH_3(g) + *$	-0.82	1.02	-0.60	1.08	-0.89	0.98	-0.16	0.00

58	$CH_3CH_2O^* + OH^* \leftrightarrow CH_3CHO^* + H_2O^*$	-0.13	0.00	-2.13	0.00	1.67	1.67	1.68	1.68
59	$CH_3CH_2O^* + ^* \leftrightarrow CH_3CHO^* + H^*$	0.36	0.78	0.03	0.37	0.37	0.87	0.27	0.34
60	$CH_3CH_2O^* + O^* \leftrightarrow CH_3CHO^* + OH^*$	1.27	1.27	0.92	0.92	1.28	1.28	0.15	0.16
61	$CH_3^* + CH_2O^* \leftrightarrow CH_3CH_2O^* + ^*$	-0.81	0.34*	-1.08	0.11*	-0.78	0.40*	0.22	0.22*
62	$CH_3^* + CHO^* \leftrightarrow CH_3CHO^* + ^*$	-1.76	0.64*	-1.09	0.95*	-1.92	0.60*	-0.67	0.00*
63	$CH_3CHO^* \leftrightarrow CH_3CHO(g) + ^*$	-2.03	0.78	-1.79	0.94	-2.17	0.67	-0.27	0.00
64	$CH_3OCH_2O^* + OH^* \leftrightarrow CH_3COOH^* + H_2O$	0.08	0.08	-2.34	0.00	1.19	1.19	2.07	2.07
65	$CH_3OCH_2O^* + O^* \leftrightarrow CH_3COOH^* + OH^*$	-0.84	0.94*	-0.84	1.01*	-0.86	0.86*	-0.02	0.00*
66	$CH_3OCH_2O^* + ^* \leftrightarrow CH_3COOH^* + H^*$	-2.02	0.23	-1.95	0.36	-2.01	0.22	-0.07	0.00
67	$CH_3O^* + CH_2O^* \leftrightarrow CH_3OCH_2O^* + ^*$	0.06	0.82	0.05	0.66	0.05	0.82	-0.14	0.00
68	$CH_3O^* + CHO^* \leftrightarrow CH_3COOH^* + ^*$	-0.68	0.47	-0.11	0.73	-0.87	0.41	-0.66	0.00
69	$CH_3COOH^* \leftrightarrow CH_3COOH(g) + ^*$	-2.16	0.00	-1.68	0.20	-2.35	0.00	-0.55	0.00

A5. Initial, Transition, and Final States of Elementary Steps

Images are not included for desorption steps.

56. $CH_3^* + CH_3O^* \leftrightarrow H_3C\text{-}OCH_3^* + {}^* \leftrightarrow CH_3OCH_3^* + {}^*$

58. $CH_3CH_2O^* + OH^* \leftrightarrow CH_3CHO\text{-}H\text{-}\text{-}OH^* + ^* \leftrightarrow CH_3CHO^* + H_2O^*$

59. $CH_3CH_2O^* + ^* \leftrightarrow CH_3CHO\text{-}H^* + ^* \leftrightarrow CH_3CHO^* + H^*$

60. $CH_3CH_2O^* + O^* \leftrightarrow CH_3CHO\text{-}H\text{-}\text{-}O^* + ^* \leftrightarrow CH_3CHO^* + OH^*$

61. $CH_3^* + CH_2O^* \leftrightarrow H_3C\text{-}CH_2O^* + ^* \leftrightarrow CH_3CH_2O^* + ^*$

62.   CH$_3$O* + CHO* $\leftrightarrow$ CH$_3$O-CHO* + * $\leftrightarrow$ CH$_3$COOH* + *

64.   CH$_3$OCH$_2$O* + OH* $\leftrightarrow$ CH$_3$OCHO-H--OH* + * $\leftrightarrow$ CH$_3$COOH* + H$_2$O*

65.   CH$_3$OCH$_2$O* + O* $\leftrightarrow$ CH$_3$OCHO-H--O*+ * $\leftrightarrow$ CH$_3$COOH* + OH*

66.   CH$_3$OCH$_2$O* + * $\leftrightarrow$ CH$_3$OCHO-H* + * $\leftrightarrow$ CH$_3$COOH* + H*

67. $CH_3O^* + CH_2O^* \leftrightarrow CH_3O\text{-}CH_2O^* + {}^* \leftrightarrow CH_3OCH_2O^* + {}^*$

68. $CH_3^* + CHO^* \leftrightarrow H_3C\text{-}CHO^* + {}^* \leftrightarrow CH_3CHO^* + {}^*$